OCEAN
ISSN 3008-1203

Open Access
Review Article

Analysis of the morphological characteristics of the Black Ghost Knifefish anal fin resulting in highly maneuverable locomotion

Ze-Jun Liang[1,2], Peng Xu[1,2] ✉, Yi-Wei Fan[3], Dong-Yang Chen[1,2], and Kun-De Yang[1,2]

[1] *Ocean Institute of Northwestern Polytechnical University, Suzhou 215400, China*
[2] *Yangtze River Delta Research Institute of Northwestern Polytechnical University, Suzhou 215400, China*
[3] *NORINCO Group Air Ammunition Research Institute Co., Ltd., Harbin 150000, China*

Cite This: *Ocean*, **2026**, *2*, 9470021

Read Online

ABSTRACT: Bionic propulsion technologies inspired by the median and/or paired fin of fish offer a promising method of addressing the limitations of traditional propeller systems in terms of low-speed maneuverability and adaptability to complex environments. This study experimentally investigated the morphological characteristics and fin kinematics of the black ghost knifefish to provide direct theoretical and data support for the design and motion modeling of bionic undulating fins. We analyzed the morphological parameters of 18 anesthetized black ghost knifefish specimens of different body lengths and 32 effective motion cases (covering nearly 2000 instantaneous moments) to systematically establish a comprehensive morphological and kinematic database for anal fin propulsion. The anal fin exhibited an arched distribution with a streamlined profile. The ratio of maximum fin height to body height was approximately 0.24, and its growth pattern conformed to the criterion of local minimization of body drag. We found that the fish achieves high maneuverability across conditions by regulating the direction of wave propagation (forward/backward) and undulation mode (unidirectional/bidirectional wave). Subsequently, key kinematic parameters were extracted and analyzed by spatiotemporal Fourier transform. The results indicated that wave frequency serves as the primary control variable for cruise speed, while wave speed, wavelength, and wave number collectively form an interrelated operational range that influence propulsion performance. The wave amplitude along the anal fin followed a typical arched nonuniform distribution, and the bidirectional wave propagation mechanism further enhanced high-maneuverability adaptation. Overall, these findings provide valuable insights into the propulsion mechanism of undulating fins that could narrow the performance gap between bioinspired robotic prototypes and their biological counterparts.

KEYWORDS: black ghost knifefish, bionic undulating fin, morphology, high maneuverability

1 Introduction

Propulsion systems, which are the core power unit of underwater vehicles, directly influence key performance metrics such as cruising speed, endurance, and acoustic signature. However, common propeller-based propulsion systems exhibit certain limitations in specific scenarios. Fish, over millions of years of natural selection and evolution, have developed a remarkable diversity in morphological structures and locomotion modes that enable them to adapt to various ecological environments. By leveraging unique motion mechanisms shaped by evolution, bionic propulsion technology offers an innovative approach to overcome the physical constraints of traditional underwater propulsion methods. Based on the primary body parts used for thrust generation, Webb classified fish swimming propulsion into two main categories: the body and/or caudal fin (BCF) mode and the median and/or paired fin (MPF) mode [1]. In the BCF mode, which is employed by approximately 85% of fish species worldwide [2], fish generate forward thrust by oscillating their body and tail fin to push water backward, utilizing the resulting reaction force. Previous studies have systematically investigated the propulsion mechanisms of BCF-mode fish across various behavioral states, including cruising swimming [2,3], escape responses [4,5], and predatory behavior [6]. Notably, the BCF propulsion mode demonstrates optimal performance during high-speed cruising in open water, but exhibits significant functional limitations in complex conditions like low-speed maneuvering, turning, and turbulent environments. In contrast, the MPF mode relies on undulations of flexible structures like the dorsal, anal, or pectoral fins to generate thrust and achieve motion control. Given the practical operational requirements of underwater vehicles, the MPF mode provides superior adaptability and performance advantages in complex aquatic environments and extreme conditions.

Within the category of MPF fish, two distinct single-fin-based propulsion modes exist: amiiform and gymnotiform locomotion. Collectively termed "ribbon-fin locomotion", these two modes are characterized by the generation of traveling waves along an elongated dorsal fin (e.g., in bowfin) and/or anal fin (e.g., in knifefish) that produce a series of propulsive waves to move the organism forward or backward. Blake [7] identified ribbon-fin locomotion as a highly efficient mechanism adapted for low-speed

Received: December 1, 2025; **Revised:** December 22, 2025
Accepted: January 12, 2026

✉Address correspondence to Peng Xu, xupeng1010@nwpu.edu.cn

swimming that exhibits superior mechanical and hydrodynamic efficiency. Among the order Gymnotiformes, the black ghost knifefish has been extensively adopted as a benchmark species for studying bionic undulating fin propulsion systems. Blake [7] and Ruiz-Torres, et al. [8] systematically investigated fin kinematics in various knifefish using high-speed videography and two-dimensional markerless motion capture systems based on fin margins. Sefati et al. [9,10] further explored the functional advantages of generating two counter-propagating waves along the anal fin; although this mechanism entails a certain trade-off in energy efficiency, they noted that it significantly enhances maneuverability and stability. The propulsion mechanism of the anal fin has been thoroughly investigated through experimental studies [11–13] and numerical simulations [14–16] of fluid dynamics. Maciver et al. [17] described the critical role of the anal fin in predatory behavior. Curet et al. [18] identified a novel vertical maneuvering behavior where counter-propagating waves are excited along the elongated anal fin to generate downward thrust, enabling vertical displacement of the fish body. Other studies have focused on the propulsion mechanisms of the anal fin in weakly electric fish, such as the black ghost knifefish, to further analyze the hydrodynamics of ribbon-fin swimming [14,19]. They found that not only does this locomotion mode provide enhanced maneuverability, it also allows the fish to maintain body rigidity while swimming. Moreover, this characteristic helps minimize electric field modulation caused by body movements to maximize various electrosensory capabilities, including foraging, intraspecific communication, and environmental sensing. Although these studies offer valuable experimental and theoretical insights, there are remaining challenges related to limited sample sizes and unverified hypotheses of the specific functions of the ribbon fin as a propulsion mechanism. Notably, a systematic and comprehensive kinematic parameter database of the anal fin motion of the black ghost knifefish has not been established, which hinders in-depth understanding and engineering applications of this propulsion mode.

The ribbon fin has also inspired robotic models employing undulatory locomotion. Prior studies [20–26] of ribbon fin motion have primarily focused on developing bioinspired robotic models, emphasizing structural design and efficiency based on this propulsion mode. Bionic undulating fin research has investigated the underlying propulsion mechanisms through two approaches: computational modeling and experimental validation. Maciver et al. [20] developed a theoretical model based on an idealized elliptical hull and a rectangular fin, revealing the multi-degree-of-freedom maneuvering potential of undulating fins at low speeds. Subsequently, Lamas et al. [21] employed computational fluid dynamics (CFD) numerical simulations to analyze fin dynamics, confirming that the magnitude and variation pattern of the angular amplitude have a critical influence on propulsion performance, with numerical results showing strong agreement with experimental measurements. Building on this ork, Zhang et al. [22] compared the propulsion effectiveness of four undulation patterns: constant amplitude, increasing amplitude, spindle-shaped, and funnel-shaped. They noted that the angular amplitude functions used in their study was idealized and did not accurately reflect the kinematic details of real biological organisms. Quan et al. [23] conducted a parametric analysis of the constant amplitude undulation mode. They identified a linear relationship between swimming speed and undulation frequency and that thrust is proportional to the square of the frequency and increases monotonically with wavelength and amplitude. Liu et al. [24] developed a robot with a single rectangular propulsion mechanism and systematically quantified the flow field structure under constant amplitude oscillations using experimental fluid methods. Bai et al. [25] applied digital particle image velocimetry to capture the dynamic phase evolution of the velocity field in both the transverse and sagittal planes during constant amplitude undulation. Shirgaonkar, et al. [14,26] utilized particle image velocimetry to observe the tethered flow field structure generated by a rectangular fin undergoing constant amplitude undulation in still water.

Despite this substantial research, existing bioinspired undulating fin prototypes lag significantly behind their biological counterparts in terms of key performance metrics like propulsion efficiency and maneuverability. Most existing studies have relied on simplified geometric models (e.g., rectangular fins) for numerical simulations and experimental analyses and employed constant amplitude undulation patterns. As these approaches fail to fully incorporate the morpho-kinematic synergistic optimization mechanisms developed by evolution, they limit further performance enhancement of bioinspired propulsion systems.

To address this research gap, this study quantifies the undulatory pattern and key kinematic parameters of anal fin propulsion in the black ghost knifefish to establish a corresponding morphology-kinematics database. Subsequently, we delve into the intrinsic mechanisms underlying its anal fin undulatory behavior and how high maneuverability is achieved. Ultimately, these findings can provide a theoretical basis for the physical model design and motion control of bionic undulating fins capable of enhancing the hydrodynamic performance of biomimetic systems and narrowing the gap with their biological prototypes.

2 Materials and methods

2.1 Choice of biological specimen

The black ghost knifefish (*Apteronotus albifrons*), shown in Fig. 1a, was selected as the focus of this study primarily due to its distinct advantages in locomotion mechanics and hydrodynamics [27,28]. First, the propulsion mode of this species in complex aquatic environments effectively reduces body drag induced by body undulation, thereby enhancing locomotion efficiency. Second, its ribbon-fin propulsion system helps minimize energy loss during low-speed swimming and shows high multidirectional maneuverability, particularly the ability to rapidly reverse swimming direction in crowded environments. Moreover, the knifefish is an ideal model for investigating neurogenic control mechanisms. The exhibited mechanical characteristics are predominantly governed by neural strategies, rather than being constrained by biomechanical structures, which is why it has been widely adopted as a canonical model system in sensory neurobiology research. Drag experienced by the knifefish during aquatic motion closely approximates the theoretical equivalent for a rigid body, reflecting high hydrodynamic efficiency and superior motion control capability. Finally, knifefish can maintain an approximately straight body posture while swimming with minimal or negligible body bending. This characteristic significantly simplifies the design and implementation of rigid-structure-based underwater undulating fins (Fig. 1b).

https://doi.org/10.26599/OCEAN.2026.9470021

2.2 Sample and morphological measurements

Eighteen black ghost knifefish specimens (purchased from an aquarium) with body lengths ranging from 52.19 to 108.48 mm were obtained to investigate the influence of individual variation and body length on morphological parameters. Prior to assessment, all fish were fasted for 6 h and selected using a random sampling method. As knifefish are live organisms with high autonomous activity, water-soluble eugenol was used as an anesthetic. This anesthetic decomposes in water and leaves no residue, ensuring that fish remained in a controllable state for a short period to facilitate accurate morphological data collection. Anesthesia was administered in a 500 mL beaker using a dropper (approximately 0.1:750 volume ratio of anesthetic to water). To minimize any adverse effects, the specific dosage was adjusted based on sample size, individual size, water temperature, and other conditions. After administering anesthesia, each fish was placed on a film grid scale for morphological imaging. The film scale served as an economical and precise measurement tool, effectively replacing expensive professional equipment to obtain reliable morphological data. To reduce shadows caused by unilateral lighting, two LED lights were symmetrically arranged on both sides of the optical platform during imaging to achieve uniform fill light. The camera (Resolution 2560 × 1600, Aperture F/2.8) was fixed horizontally directly above the platform. After imaging, each fish was immediately transferred to clean water for recovery (consciousness was typically regained in approximately 5 min). After all 18 specimens had been measured, they were observed under captive conditions for 2 weeks. No behavioral or health abnormalities were noted during this period. The overall setup for morphological measurements and a schematic of morphological imaging on the film grid scale are shown in Fig. 2.

The obtained images were analyzed using ImageJ software as follows. Calibration was performed using tools within the software. A grid line segment of known length in the image was selected to determine the physical dimensions represented by each pixel. This calibration step transformed the image coordinates from a pixel-based system to a millimeter-based system and was the foundation for all subsequent measurements. After calibration, the software's built-in edge detection algorithm with subpixel accuracy was utilized to identify key points along the specimen's contours. By analyzing grayscale transitions between pixels, these algorithms enhance edge localization precision to the subpixel level. The software then calculated the actual physical distances between these coordinate points based on the calibration factor. The measurement values used in our analyses were derived from repeated measurements performed on multiple independently captured images (n = 5). The standard deviation (SD) of these measurements reflects the combined precision accounting for minor inherent sample variation and the reproducibility of our methods.

2.3 Kinematic measurements

The same 18 black ghost knifefish used for the morphological assessment were selected for kinematic observations. The experiments were conducted in a custom-built transparent aquarium measuring 600 mm × 400 mm × 600 mm (length × width × height) with a maintained water depth of 100 mm, as shown in Fig. 3a. Because knifefish are sensitive to water quality, the pH was maintained at 6.5 ± 0.3, hardness at 7 ± 4 dH, and water temperature at 25 ± 2°C throughout the experimental period. To allow for environmental acclimation and minimize the impact of external disturbances on fish behavior, the specimens were introduced into the experimental water 24 h prior to formal testing. The handling time for each fish during capture was limited to a maximum of 10 min to ensure data accuracy. After handling, a recovery period of 5–10 min was allowed to prevent behavioral deviations caused by fatigue.

To enable multiangle synchronous recording, we used a motion

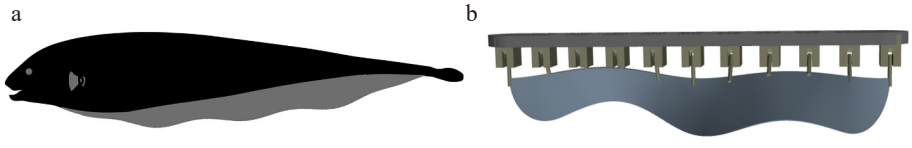

Figure 1 Focal fish of the present study and the bionic undulating fin model (mimicking the anal fin of the black ghost knifefish). (a) Aquatic organism (black ghost knifefish). (b) Bionic undulating fin model.

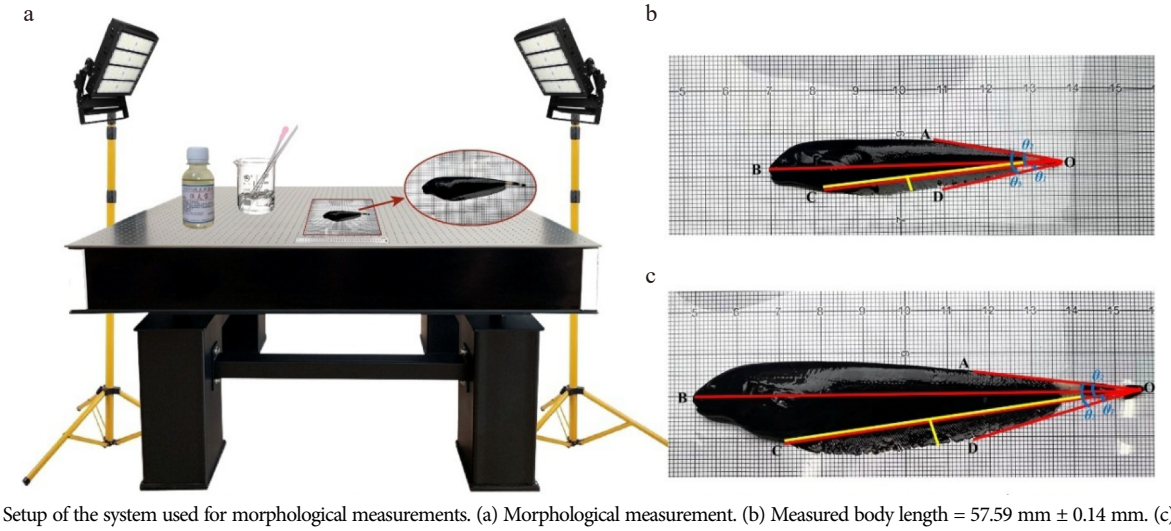

Figure 2 Setup of the system used for morphological measurements. (a) Morphological measurement. (b) Measured body length = 57.59 mm ± 0.14 mm. (c) Measured body length = 108.48 mm ± 0.18 mm.

capture system consisting of three high-speed cameras connected to a computer via a high-precision synchronizer. The three cameras were positioned above, below, and to the side of the aquarium. The top and bottom cameras were used to capture the motion characteristics of the fish body axis and anal fin from the dorsal and ventral views. The lateral camera served as the primary viewpoint for monitoring whether the anal fin boundary remained parallel to the horizontal plane, thereby ensuring the geometric validity of the dorsal and ventral view data. To enhance image quality, two LED lights were symmetrically arranged on both sides of the optical platform to provide uniform fill lighting. This reduced shadow interference and ensured clear visibility of the fish body contour and anal fin boundary. The instantaneous morphological characteristics of the fish from the dorsal and ventral views are shown in Figs. 3b and 3c, respectively. The dorsal view reveals the fish's streamlined body shape, which helps reduce fluid resistance during swimming. A bottom view image shows that the anal fin projection is located on the body's axis of symmetry and undulates around the central axis. This bilaterally symmetrical body structure is conducive to maintaining balance and avoiding yaw during locomotion.

A high-resolution digital camera was used to visually record the swimming sequences. A total of 32 valid motion cases were captured at a frame rate of 400 frames per second, comprising eight cases each for forward and backward swimming for small-sized individuals and eight cases each for forward and backward swimming for large-sized individuals. To facilitate analysis, a unified naming convention was adopted using the formats S_F_*n*, S_B_*n*, L_F_*n*, and L_B_*n*, where S denotes small size, L denotes large size, F represents forward swimming, B represents backward swimming, and *n* is the case sequence number (n = 1–8). As the fish are live organisms exhibiting autonomous behavior and the camera's field of view was limited to an area of 180 mm × 150 mm, the acquisition duration varied across cases. The capture time for the 32 cases ranged between 125 and 1,000 ms.

3 Results and discussion

3.1 Analysis of morphological characteristics

The morphological parameters of one knifefish specimen from each size group are shown in Fig. 4. The line segments in the figure are defined as follows: OA represents the line connecting the caudal fin tip and the dorsal contour; OB represents the body length, connecting the snout and the caudal fin tip; OC denotes the line between the caudal fin tip and the extended baseline of the anal fin (with yellow solid lines indicating the length and width of the anal fin); and OD represents the line connecting the caudal fin tip and the anal fin boundary. The angles between these line segments characterize the fish's morphological parameters: θ_1 represents the angle between the anal fin boundary and the extended baseline of the anal fin; θ_2 represents the angle between the dorsal contour line and the extended baseline of the anal fin; and θ_3 represents the angle between the dorsal contour line and the anal fin boundary.

Table 1 summarizes the measured morphological parameters for

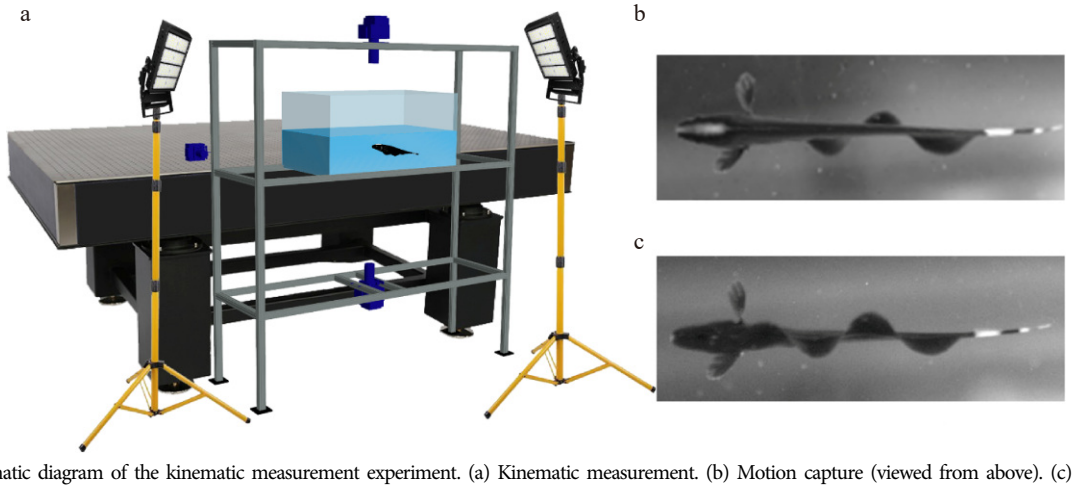

Figure 3 Schematic diagram of the kinematic measurement experiment. (a) Kinematic measurement. (b) Motion capture (viewed from above). (c) Motion capture (viewed from below).

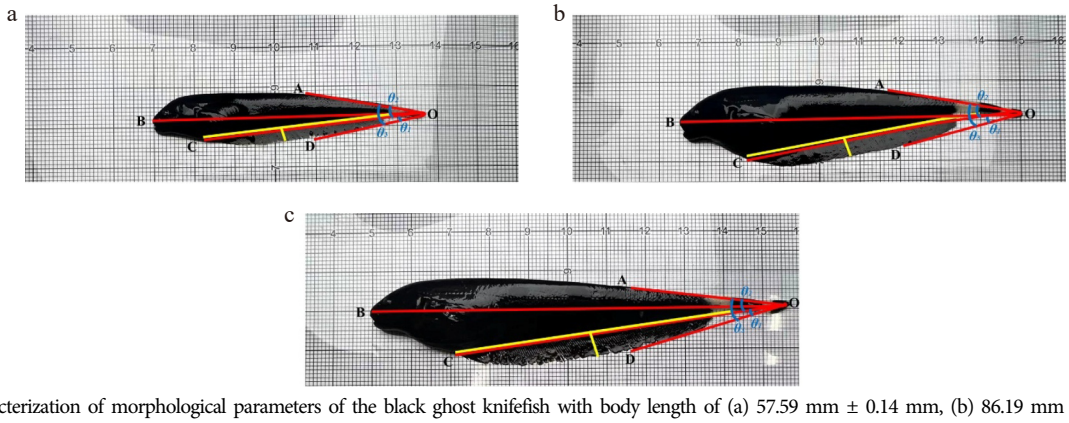

Figure 4 Characterization of morphological parameters of the black ghost knifefish with body length of (a) 57.59 mm ± 0.14 mm, (b) 86.19 mm ± 0.21 mm, and (c) 108.48 mm ± 0.18 mm.

black ghost knifefish. Although the external morphological parameters of different individuals and size groups did not exhibit clear patterns, all values fell within certain ranges, indicating a degree of stability in morphological characteristics. Notably, there are several potential sources of error in our measurement process [29]: 1) the limited sample size (n = 18), which may have included morphologically atypical individuals; 2) the limited time available to position the anesthetized fish out of water could lead to positional and angular deviations on the grid paper; and 3) manual tracing for angle extraction may have introduced a degree of subjective error. Despite these potential error sources, our study yielded the following morphological findings: the angle between the anal fin boundary and its extended baseline (θ_1) ranged from 9.78° to 10.32°; the angle between the dorsal contour line and the extended anal fin baseline (θ_2) ranged from 12.56° to 13.53°; and the angle between the dorsal contour line and the anal fin boundary (θ_3) ranged from 22.81° to 23.68°. The starting position of the anal fin largely coincided with the location of the fish's maximum body width. The aforementioned range closely aligns with findings from Ruiz-Torres et al. [8] and Youngerman et al. [30].

The morphological experiments revealed that the black ghost knifefish possesses a blade-like abdominal structure that gradually tapers toward the tail. Its propulsion system primarily comprises the anal fin (main propulsive organ), pectoral fins (auxiliary for balance, not a primary propulsion source), and a reduced caudal fin; dorsal and pelvic fins are entirely absent. This configuration represents a typical morphological adaptation of the knifefish to its aquatic environment [31].

Next, we focus on the primary propulsive organ, the anal fin. The anal fin presents as an elongated ribbon-like structure that extends up to three-quarters of the body length. The maximum body depth is located at the vertical transverse plane through the distal edge of the pectoral fin. The anal fin originates near the base of the pectoral fin and extends to a position close to the reduced caudal fin. Although the fin is predominantly black in coloration, the anal fin gradually becomes transparent approximately 1 cm from the tail end, forming a distinct white band at the terminus. To investigate patterns of anal fin width, we selected 6 specimens each from the small (body length: 52.19–57.59 mm), medium (body length: 77.54–86.19 mm), and large (body length: 104.44–108.48 mm) size groups. The anal fin boundaries were digitally extracted and the results are presented in Fig. 5. To enhance the representativeness and generalizability of the findings, the digitized samples covered three scenarios: same body lengths and same individuals (Fig. 5a), same body lengths but different individuals (Fig. 5b), and different body lengths and different individuals (Fig. 5c). Due to physiological and morphological variation among individuals in the same size group, the anal fin width data exhibited fluctuations within a very narrow range and did not completely overlap. Overall, the knifefish anal fin follows an arched distribution. The digitized fin width profile show a unimodal pattern: for individuals of the same size, the anal fin width gradually increases, fluctuates near the peak, and then gradually decreases. This distribution characteristic contributes to maintaining a streamlined body profile. The overall fin profile is bilaterally symmetrical about the central baseline, and the maximum fin width increases with body length. The ratio of the maximum fin height to body height was approximately 0.24, and its growth pattern conforms to the criterion of local minimization of body drag.

3.2 Analysis of high-maneuverability mechanisms

3.2.1 Data preprocessing

The black ghost knifefish primarily employs undulations of its anal fin to achieve various locomotion modes. This anal fin originates near the insertion point of the pectoral fin and extends toward the

Table 1 Detailed list of morphological parameters.

Specimen number	Body length/mm	θ_1/(°)	θ_2/(°)	θ_3/(°)	Maximum fin width h/mm
1	52.19 ± 0.85	9.78 ± 0.12	13.14 ± 0.08	22.92 ± 0.21	3.75 ± 0.39
2	52.26 ± 1.02	10.12 ± 0.37	12.98 ± 0.12	23.10 ± 0.13	3.77 ± 0.41
3	53.13 ± 0.93	9.86 ± 0.14	13.27 ± 0.16	23.13 ± 0.34	3.82 ± 0.58
4	53.88 ± 0.62	9.94 ± 0.16	13.32 ± 0.23	22.81 ± 0.18	3.91 ± 0.62
5	54.37 ± 0.68	10.09 ± 0.14	13.52 ± 0.18	23.61 ± 0.12	3.95 ± 0.38
6	57.59 ± 0.91	10.06 ± 0.23	12.56 ± 0.09	22.85 ± 0.37	4.19 ± 0.74
7	77.54 ± 0.23	10.21 ± 0.16	13.01 ± 0.08	23.22 ± 0.14	4.85 ± 0.58
8	78.89 ± 0.67	10.16 ± 0.21	12.93 ± 0.11	23.09 ± 0.56	5.06 ± 0.32
9	79.45 ± 0.45	10.27 ± 0.30	13.40 ± 0.20	23.67 ± 0.24	5.25 ± 0.41
10	79.61 ± 1.12	10.15 ± 0.18	13.06 ± 0.12	23.21 ± 0.37	5.31 ± 0.52
11	80.96 ± 1.03	9.98 ± 0.23	13.23 ± 0.24	23.19 ± 0.25	5.89 ± 0.25
12	86.19 ± 0.77	10.02 ± 0.13	12.94 ± 0.11	23.24 ± 0.22	6.69 ± 0.18
13	104.44 ± 0.81	10.24 ± 0.21	12.89 ± 0.21	23.13 ± 0.31	7.73 ± 0.74
14	104.85 ± 0.94	10.17 ± 0.18	13.10 ± 0.14	23.21 ± 0.28	8.07 ± 0.53
15	105.88 ± 0.86	10.21 ± 0.09	13.37 ± 0.16	23.58 ± 0.18	8.17 ± 0.46
16	106.91 ± 1.08	10.32 ± 0.14	13.30 ± 0.05	23.62 ± 0.86	8.25 ± 0.38
17	107.67 ± 1.23	10.15 ± 0.23	13.53 ± 0.14	23.68 ± 0.54	8.31 ± 0.27
18	108.48 ± 0.91	9.96 ± 0.28	12.99 ± 0.07	23.29 ± 0.27	8.38 ± 0.42

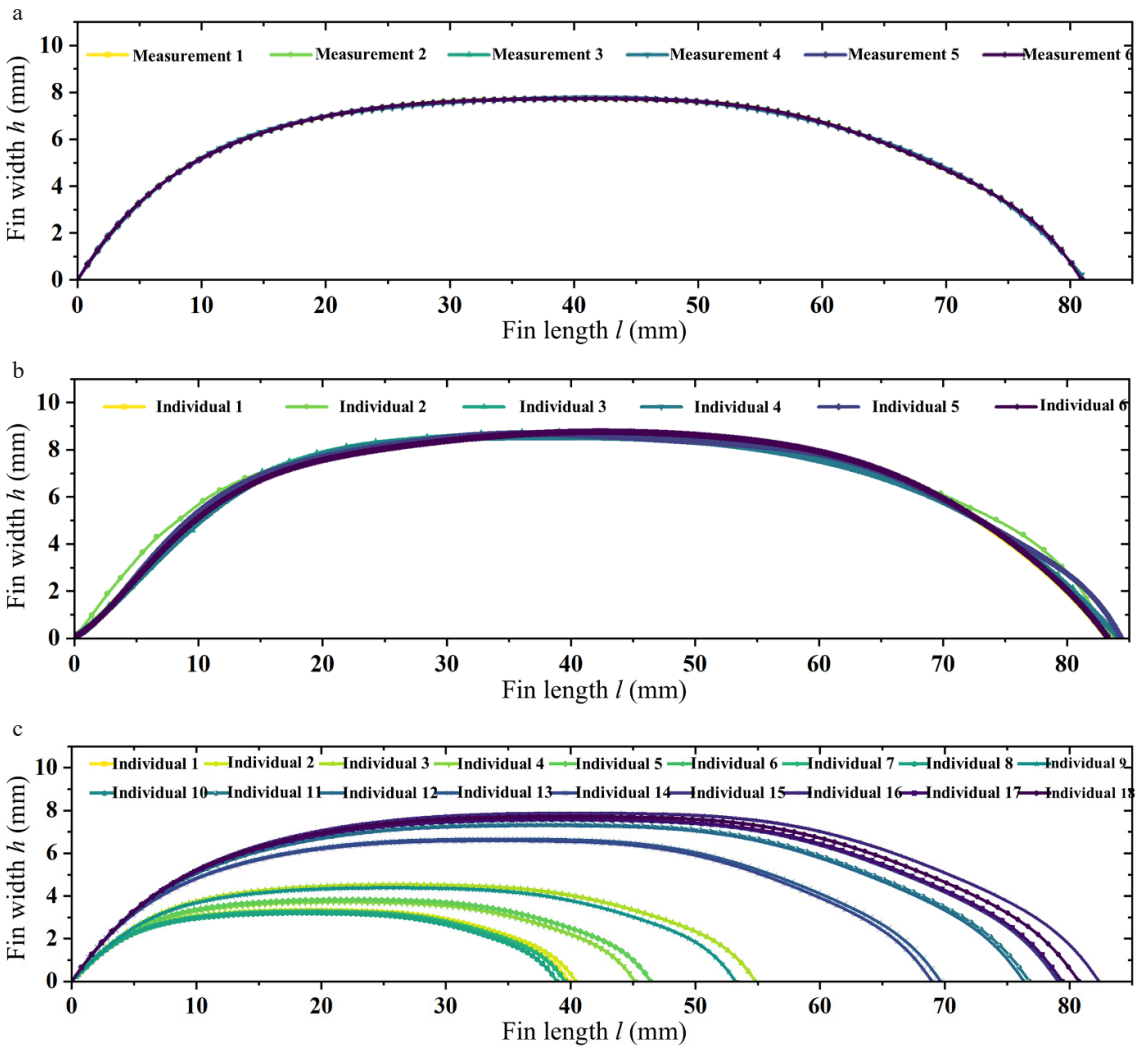

Figure 5 Digitized results of anal fin width. (a) Same body lengths, same individuals. (b) Same body lengths, different individuals. (c) Different body lengths, different individuals.

region of the reduced caudal fin. To quantitatively analyze the undulation characteristics of the anal fin boundary, we digitally extracted the outer edges. Due to similar coloration between the anal fin and body and the consequent lack of distinct features for deep learning-based methods, digital reconstruction of the anal fin boundary was achieved by manual tracing of key points combined with cubic spline fitting. This approach also enabled accommodation of the waveform complexity along the fin edge. Prior to analysis of the kinematic characteristics, the digitized results for the anal find were preprocessed as follows: 1) correction of the pitch and yaw angles of the anal fin boundary; 2) adjustment of the projection of the central axis connecting different wave segments of the anal fin within the image plane to approximate a straight-line distribution; and 3) supplementing the positions of the first and last points by interpolation to ensure consistent fin edge length across all frames within a single operational case.

Figure 6 illustrates two typical motion states of the anal fin from the primary perspective of the lateral camera: the presence of a pitch angle α (Fig. 6a) and the presence of a yaw angle β (Fig. 6b). Although the fin may appear to exhibit a nearly straight undulation pattern in the dorsal and ventral views, the presence of a pitch angle in the anal fin boundary introduces error in the waveform data related to cos α. Accordingly, we applied horizontal correction to cases with a pitch angle to obtain anal fin undulation data that more closely reflects the true swimming state. The yaw angle is defined as the angle between the line connecting the snout and tail peduncle end and the horizontal direction. In the ventral view, the yaw angle has a relatively minor impact on the accuracy of the undulation data. However, to establish a unified mathematical model of anal fin undulation, a consistent coordinate system must be defined. To do so, we calculated the rotation angle based on the straight line determined by the first and last points at each time instance and achieved coordinate system unification across all operational cases through coordinate rotation.

In kinematic analysis, merely correcting the pitch or yaw angles of the anal fin boundary is insufficient to meet the processing requirements for all experimental data. Due to the autonomous nature of fish swimming, body flexion may occur under certain operational conditions. This causes the central axis connecting individual wave segments along the fin edge to deviate from a straight line, compromising the accuracy of anal fin undulation characterization. Although pitch angle correction can improve data quality to some extent, it does not guarantee that the wave projection is perfectly straight in the horizontal plane across all

cases. Figure 7 shows an instantaneous swimming state of a black ghost knifefish simultaneously captured by three cameras. To further enhance data reliability, we selected morphological characteristics at a representative time instance and compared the digital reconstruction of the anal fin edge before and after preprocessing (Fig. 8). During digitization, the number of central axis points depends on the number of wave segments (red areas in Fig. 8a represent waves formed by anal fin undulation). The start and end points of each wave are defined as key points of the central axis (marked by yellow hollow circles in Figs. 7 and 8), while the blue curves represent the digitized results of the anal fin edge and its central axis. Deviations in the line connecting the start and end points of each wave segment were observable in both the lateral and ventral views: inconsistent angles with the horizontal axis were observed in the lateral view and deviation from the ideal central axis (red dashed line) in the ventral view. Figures 8c and 8d present a comparison of the digitized wave edges before and after preprocessing. After preprocessing, the lines connecting the start and end points of each wave segment aligned more closely with the central axis, indicating improved accuracy and consistency of the kinematic data.

Figure 9 presents the preprocessing workflow using an example boundary contour of the anal fin at a representative time instance. Because the distal portion of the anal fin extends into the region of the reduced caudal fin, which is located at the transition between black and white coloration, the contour vertices in this area can be manually identified with relatively high accuracy across consecutive time frames. Leveraging this characteristic, we used two central axis points near the tail end (i.e., the distal part of the anal fin) as a reference. By calculating the angle between the line connecting

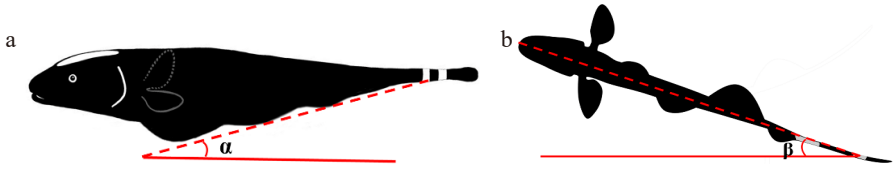

Figure 6 Motion states prior to correction. (a) Pitch state. (b) Yaw state.

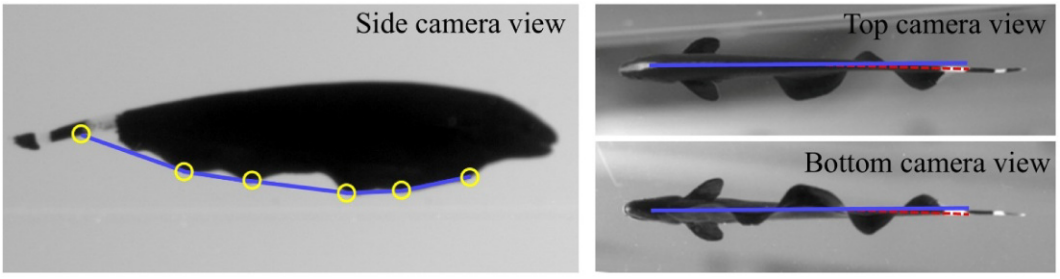

Figure 7 Morphological characteristics from different camera perspectives.

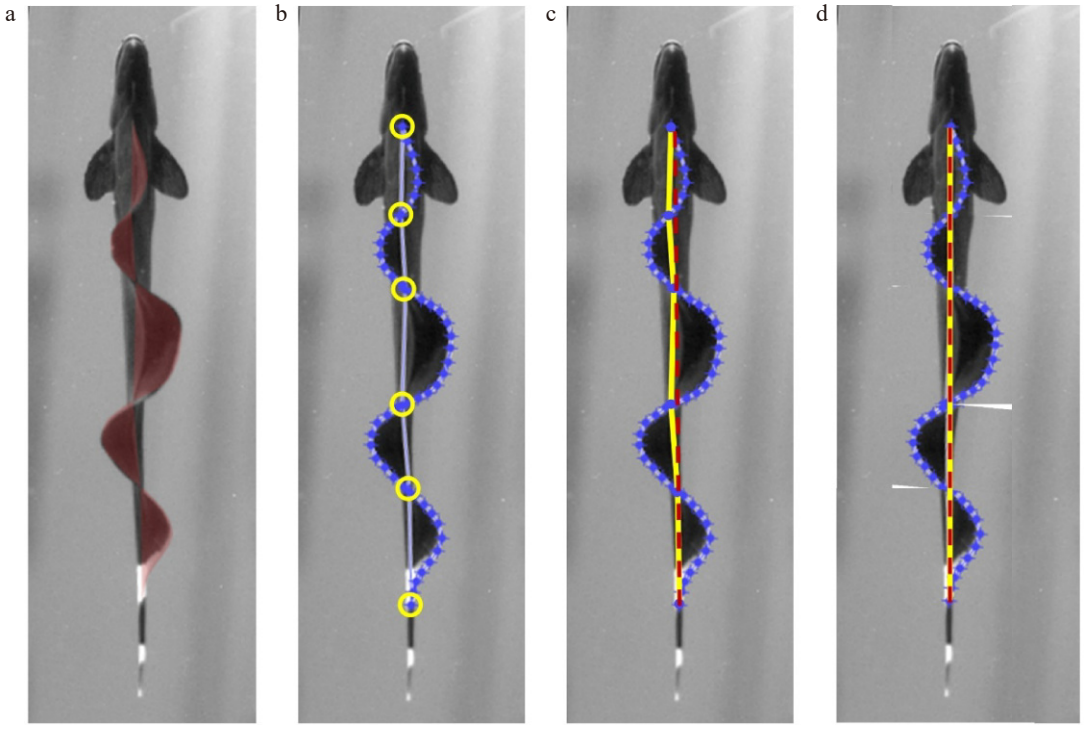

Figure 8 Digitization of the anal fin edge before and after preprocessing correction. (a) Waveform. (b) Central axis point. (c) Before preprocessing. (d) After preprocessing.

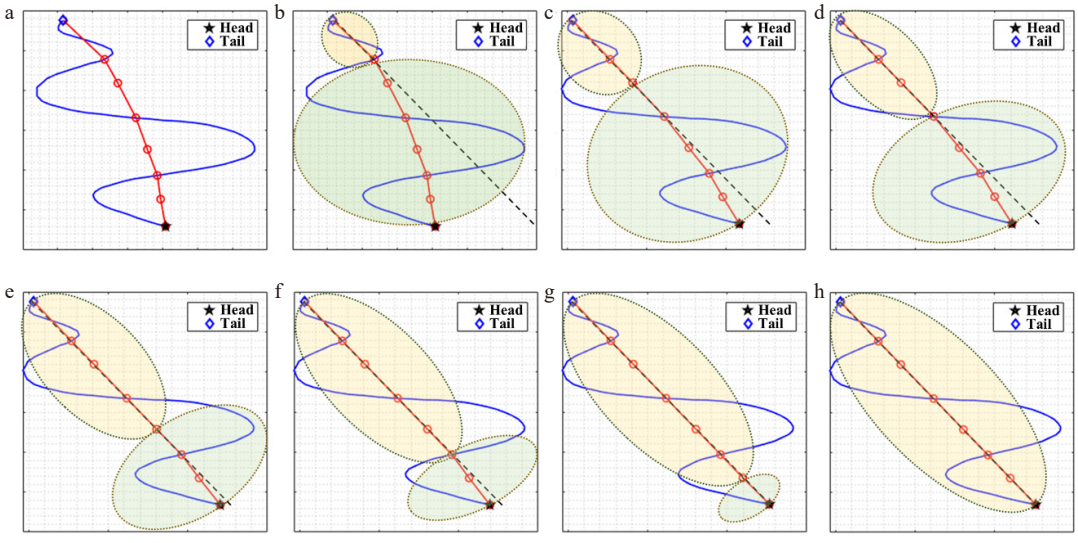

Figure 9 Workflow for correcting anal fin edge data. Original image (a), the 1st (b), 2nd (c), 3rd (d), 4th (e), 5th (f), 6th (g), and 7th (h) iteration. The blue line represents the digitized anal fin edge and the red hollow circles and their connecting lines denote the start/end positions and central axis of each wave segment, respectively.

these points and a horizontal reference line (black dashed line), an iterative algorithm was applied for linearization correction of all fin line data. As the number of central axis points corresponding to the anal fin waves varies across operational cases, the number of iterations is dynamically determined by the actual situation (e.g., 7 iterations were performed for the instantaneous case shown in Fig. 9). The yellow shaded areas in the figure indicate the corrected wave segments, whereas the green areas represent those awaiting correction. After this processing, the lines connecting the start and end points of each wave segment aligned more closely with the central axis, further enhancing the accuracy of kinematic parameter extraction.

During this digital tracing process, we adhered to the fundamental principle of not significantly deviating from the actual fin edge contour. As the distal portion of the anal fin extends into the region of the reduced caudal fin, which is located at the black-and-white color boundary with relatively distinct features, relatively accurate manual identification across consecutive frames was possible. However, because the proximal end of the anal fin (near the head) exhibits similar coloration to the body and lacks distinct morphological features, this may lead to certain localization errors that, in turn, result in inconsistency in the distance between the line connecting the first and last points across instantaneous frames. To eliminate this error, we statistically analyzed the maximum and minimum distances between the first and last points of the anal fin edges at different instances across all 32 operational cases. Using the relatively stable distal vertex from the digitized results as an alignment reference, we applied a linear interpolation method. Using the maximum first-to-last point distance recorded in a specific case as the reference, the fin edge position data were aligned and adjusted frame-by-frame. This procedure fixes both the tail and head ends at predefined positions and orientations, ensuring that the fin's projection in the image plane follows a straight-line distribution with a unified length equal to the maximum first-to-last point distance for that case. Notably, all calculations involving fin length are based on direct measurement of the fin base insertion length of anesthetized specimens, not the edge length extracted from digitized videos. Because the fin edge length undergoes fluctuations with changes in wave amplitude, it is unsuitable as a morphological benchmark.

The aforementioned preprocessing primarily consisted of the following operations: processing the pitch and yaw angles of the anal fin contour line (data rotation); adjusting the projection of the central axis connecting different wave segments within the image plane to achieve a straight-line distribution (projection correction); aligning the tail points of the rotated data within a single operational case (data alignment); and supplementing the positions of the first and last points via interpolation to ensure consistent fin edge length across all frames for a given case (data interpolation).

Our subsequent analyses focused on the undulation characteristics and quantitative parameters of the anal fin contour line. To accurately reflect the natural swimming state of the fish when analyzing undulation properties, only data rotation and projection correction were applied. An example of the resulting edge contours is shown in Fig. 10 (using case L_F_2). To eliminate the influence of swimming displacement on the spatiotemporal Fourier transform results, complete data alignment and interpolation procedures were performed. An example of the contour data after this full processing is shown in Fig. 11 (using case L_F_2).

3.2.2 *Kinematic characteristics of the anal fin*

Our motion capture data showed highly consistent swimming patterns and undulation kinematics across black ghost knifefish from different size groups. Accordingly, we randomly selected tworepresentative cases from the 32 valid operational cases (covering nearly 2000 instantaneous moments) for presentation. The motion morphologies for these cases are shown in Figs. 12–14. In contrast to the kinematic patterns observed in previous studies of undulatory locomotion in fish where a single bending wave propagates along the body from head to tail and speed modulation is primarily driven by changes in the frequency of bending [32], the black ghost knifefish exhibits bidirectional traveling waves with nodal points [18,33]. We observed that a knifefish can propel itself during forward and backward swimming with minimal or no body bending, effectively reducing body drag induced by body oscillation. This characteristic provides a biological reference for simplified robotic design based on a rigid hull structure. Among knifefish, propulsion is primarily achieved through undulations of the anal fin. By modulating parameters such as wave amplitude,

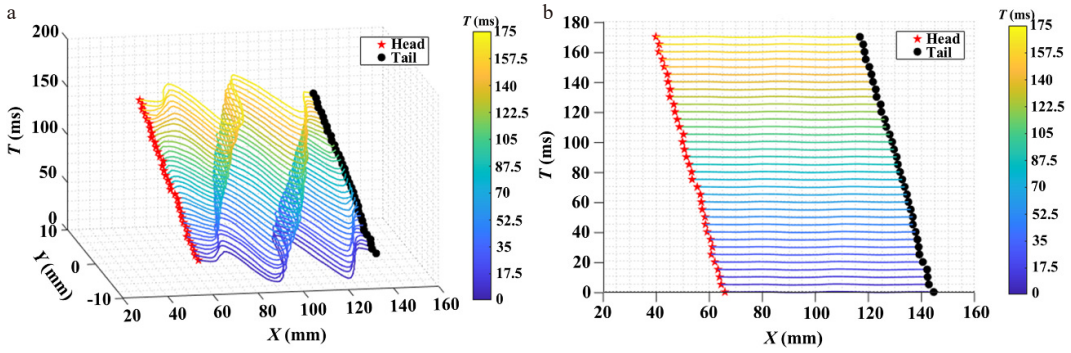

Figure 10 Edge contour line data processing (rotation and correction operations). (a) Temporal plane position. (b) Temporal projection position of the *X* direction.

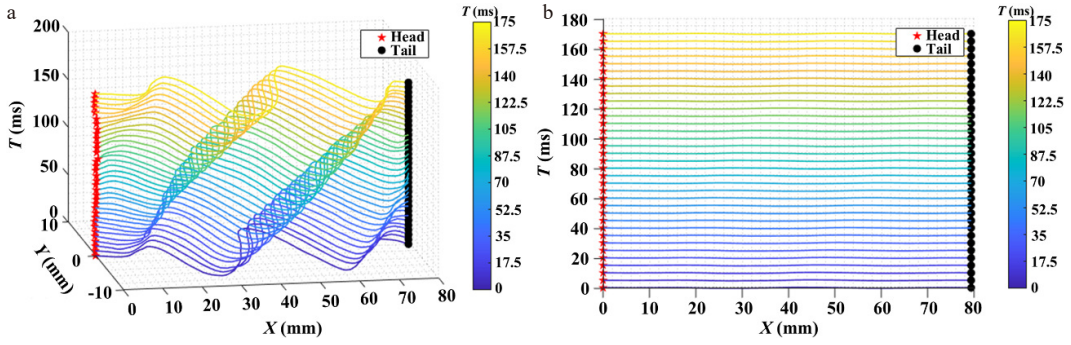

Figure 11 Edge contour line data processing consisted of rotation, correction, alignment, and supplementation operations. (a) Temporal plane position. (b) Temporal projection position of the *X* direction.

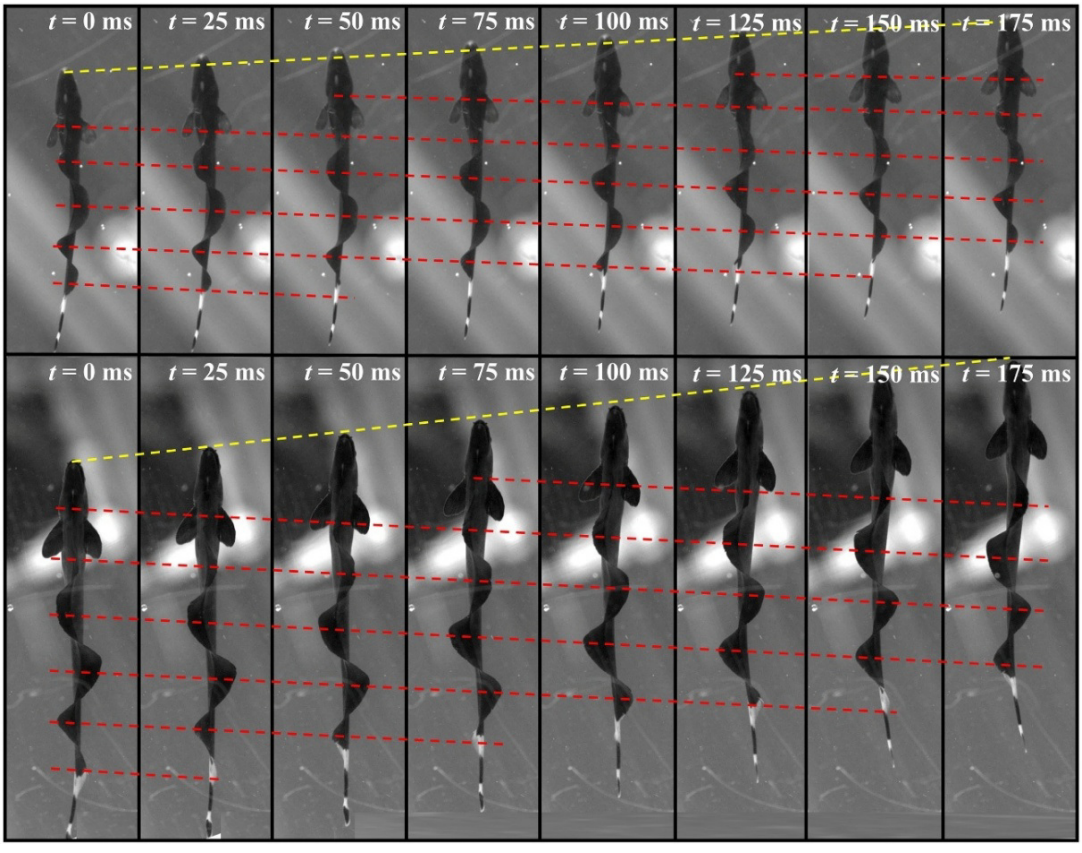

Figure 12 Forward morphology of the black ghost knifefish. Upper panels: small size specimen; lower panels: large size specimen.

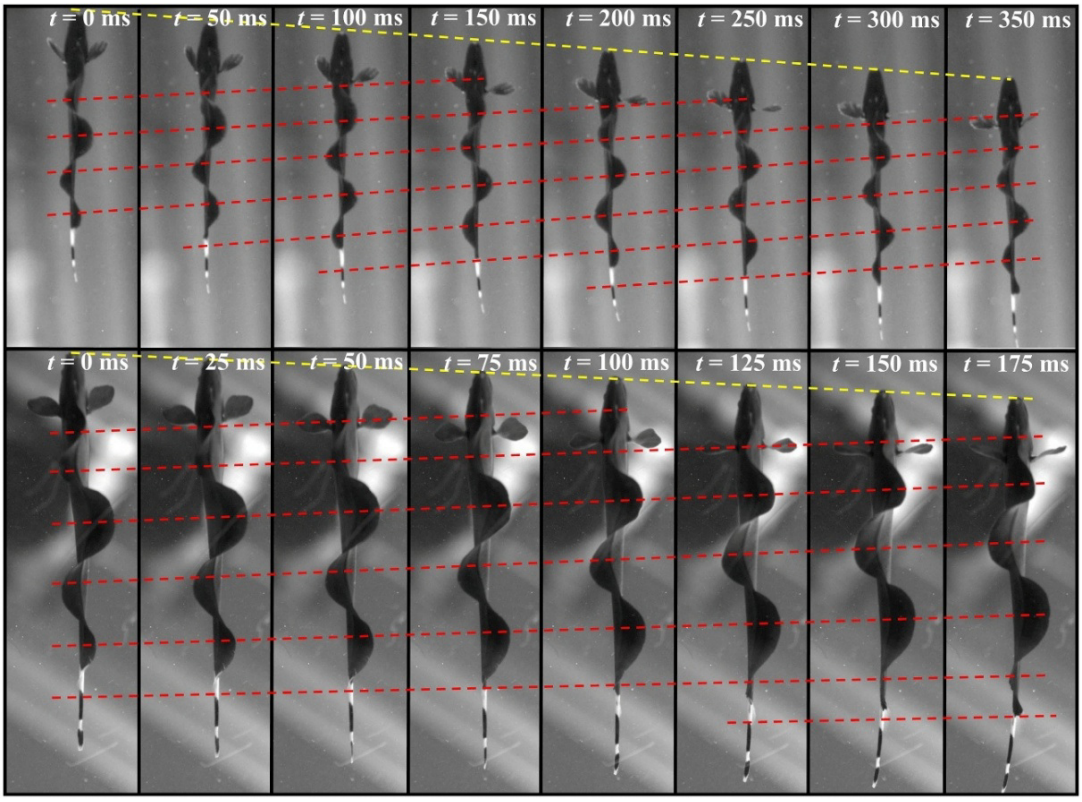

Figure 13 Backward morphology of the black ghost knifefish. Upper panels: small size specimen; lower panels: large size specimen.

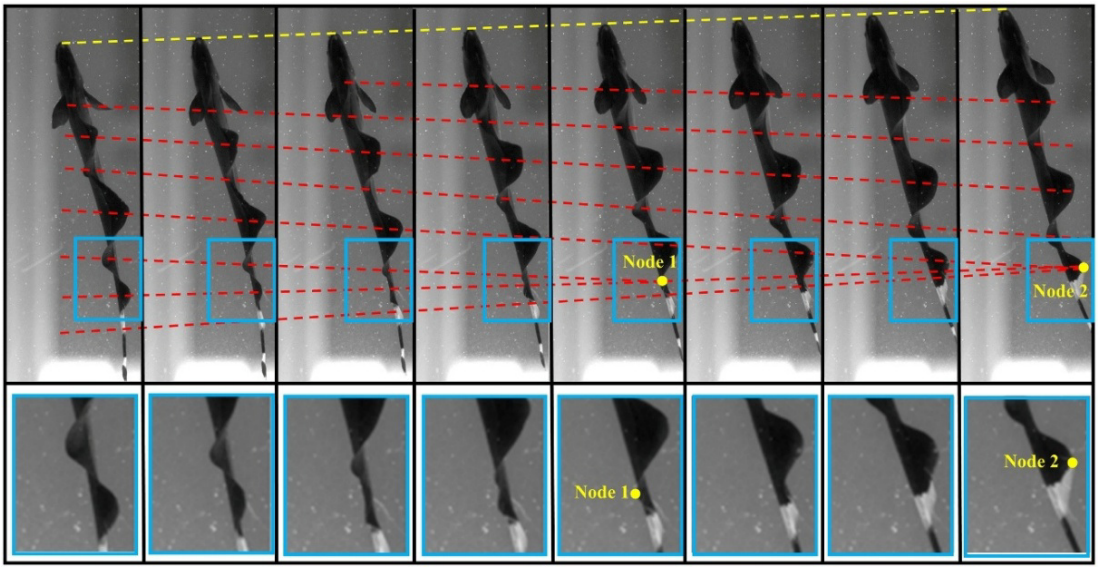

Figure 14 Slow forward morphology of the black ghost knifefish, showing both head and tail waves.

wave number, wavelength, and frequency, knifefish can perform backward swimming without a turning maneuver, resulting in high multidirectional maneuverability and rapid motion mode switching capability. During forward swimming (yellow dashed line, Fig. 12), undulations of the anal fin boundary are generated at the anterior end and propagate backward along the fin surface (red dashed line, Fig. 12). In contrast, during backward swimming (yellow dashed line, Fig. 13), waves are generated at the posterior end and propagate forward (red dashed line, Fig. 13). During slow forward swimming (yellow dashed line, Fig. 14), we observed that two counter-propagating traveling waves can simultaneously coexist on the anal fin—one moving from head to tail and the other from tail to head. These waves meet at a specific point on the fin, defined as the node (yellow solid circle, Fig. 14). The partial force cancellation resulting from these counter-propagating waves (red dashed line, Fig. 14) result in a significant reduction in swimming speed, potentially causing a hovering state. These findings regarding the movement characteristics of the black ghost knifefish are consistent with reports from Ruiz-Torres et al. [8] and Youngerman et al. [30]. Through this phenomenon, black ghost knifefish can precisely control their swimming direction and speed by regulating the propagation direction and kinematic parameters of the traveling waves on its anal fin. As the movement patterns and propulsion mechanisms were highly consistent across specimens of different

https://doi.org/10.26599/OCEAN.2026.9470021

sizes, this suggests a universal principle. Regarding the auxiliary role of the pectoral fins, we observed the following: during forward cruising, they remain closely appressed to the body sides without significant movement while, during backward swimming, they exhibit pronounced forward sweeps. These findings indicate that propulsion is primarily generated by anal fin undulations, whereas the pectoral fins are mainly utilized for posture adjustment. The undulations generated by the anal fin may be unidirectional or bidirectional. By flexibly adjusting the kinematic parameters of single or dual waves in response to changes in the fluid environment, knifefish achieve highly maneuverable and multidirectional locomotion.

Accurate extraction of the contour lines of the anal fin at each instantaneous moment during swimming is fundamental for analysis of locomotion characteristics. Figure 15 and 16 present the waveform contour lines of the anal fin during backward and forward swimming, respectively, based on the 32 valid operational cases collected in this study (comprising nearly 2000 instantaneous moments). In these figures, subpanels (a) to (h) represent eight cases of small-sized individuals while subpanels (Ⅰ) to (Ⅷ) represent eight cases of large-sized individuals. The colors of the curves indicate the spatial undulation positions of the anal fin at

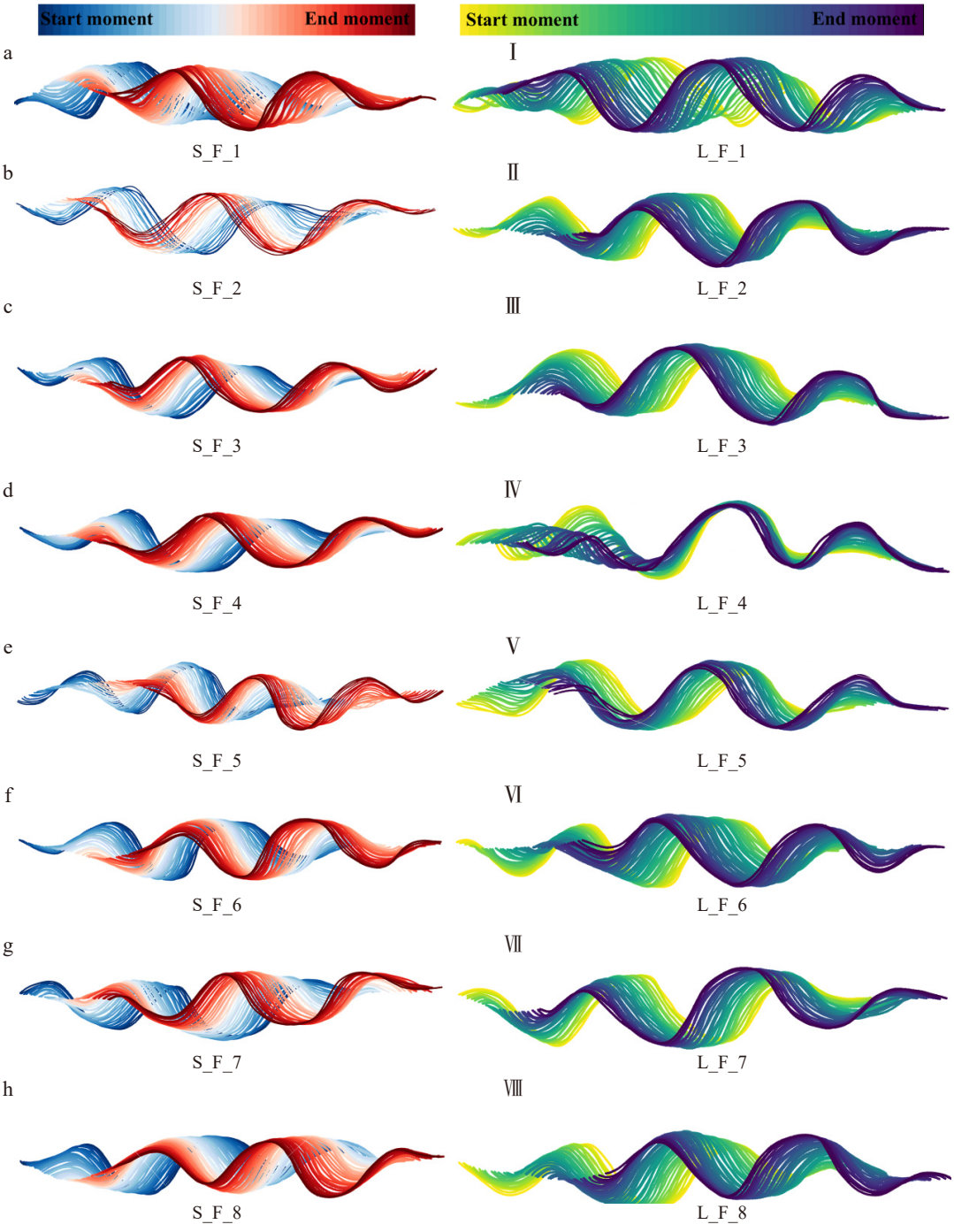

Figure 15 Anal fin boundary outline. Forward swimming, the curves of different colors represent the fluctuating positions of the hip fin in space at different moments, and the number of colors reflects the capture duration of this condition.

different times, with the number of colors reflecting the capture duration for each case. To more clearly illustrate the wave propagation direction, only the start and end positions are marked on the scale bar. Overall, we observed that the anal fin of exhibits a typical wavelike morphology during both forward and backward swimming, characterized by spatiotemporally dynamic curves that resemble basic trigonometric functions. However, a visual comparison of wave amplitude and wavelength across cases reveals that anal fin undulation does not conform to a standard sinusoidal or cosinusoidal pattern. Significant differences in waveform parameters were present between different operational cases, and their specific parametric expressions also varied. We further explore the potential relationship between undulation parameters and swimming performance later in this study. Further comparison between Figs. 15 and 16 reveal that the undulation amplitude along the anal fin boundary during swimming generally follows a distribution pattern of being smaller at both ends and larger in the middle. Furthermore, the peak of the propulsion wave within the anal fin waveform contour can deviate from a central position. The direction of this offset is opposite to the swimming direction, resulting in a relatively gentle ascending phase and a steeper descending phase along the wave propagation direction, reflecting a pattern of asymmetric morphology.

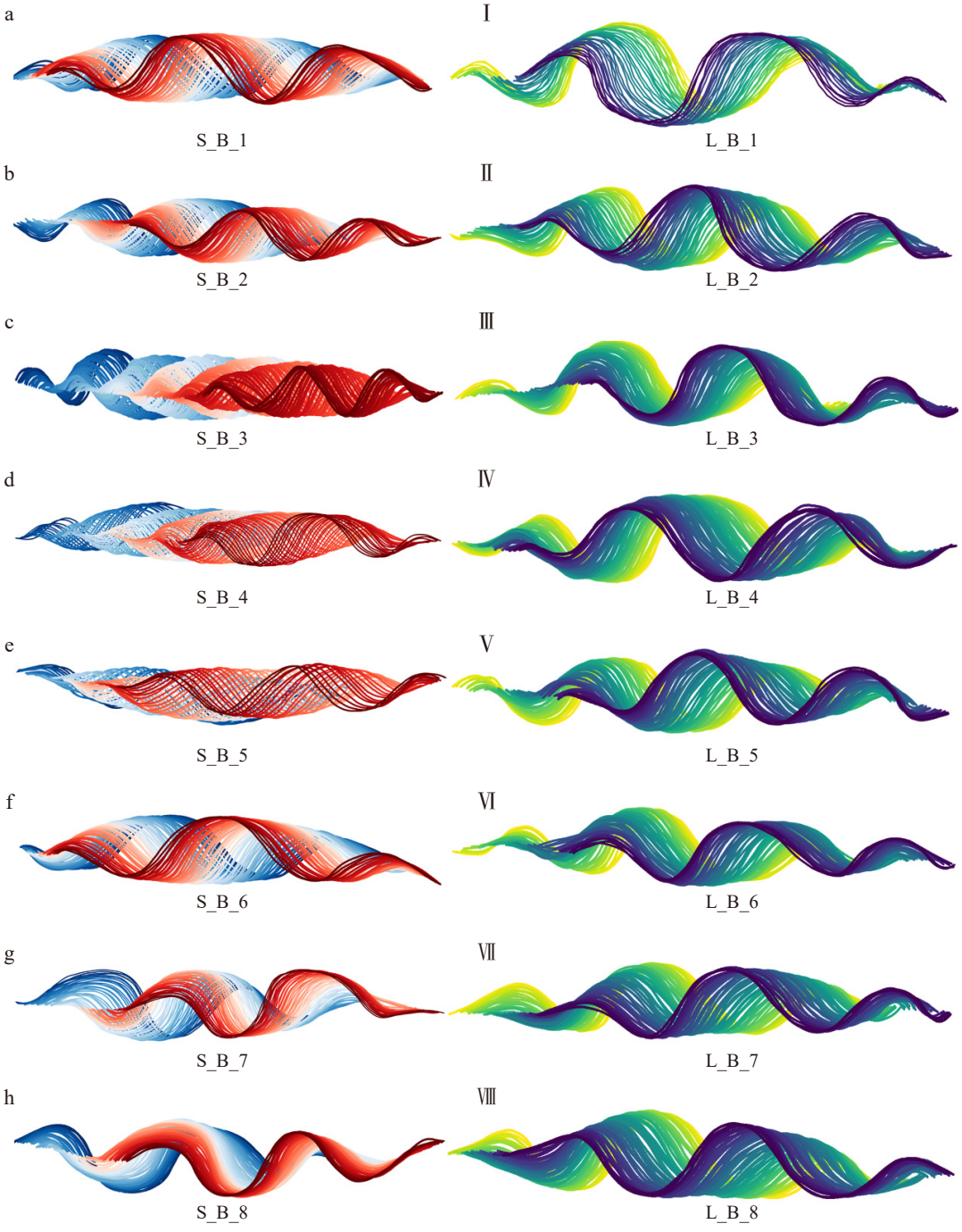

Figure 16 Anal fin boundary outlines. Backward swimming, the curves of different colors represent the fluctuating positions of the hip fin in space at different moments, and the number of colors reflects the capture duration of this condition.

https://doi.org/10.26599/OCEAN.2026.9470021

3.2.3 *Quantitative analysis of undulation parameters*

The anal fin of the black ghost knifefish exhibits distinct time-varying dynamic undulation characteristics while swimming, with its kinematic parameters at various points continuously changing over time. The resulting undulatory curve is not an ideal trigonometric function; rather, it is a waveform with a degree of irregularity. To analyze these nonstandard waveforms, we employed the Fourier transform method to facilitate conversion of signals between the temporal (or spatial) and frequency domains. The temporal Fourier transform converts time-series data into a frequency-domain representation to reveal its temporal frequency composition. Conversely, the spatial Fourier transform uses spatial position as the independent variable, and its output corresponds to the spatial frequency components of the waveform. As the input data, we used the anal fin edge contour lines after rotation, correction, alignment, and interpolation processing. This approach ensures alignment of the waveform tails and uniform length supplementation based on the maximum length, satisfying the data requirements for Fourier analysis. A total of 32 valid operational cases were collected. To illustrate the Fourier transform analysis procedure, Fig. 17 presents the coordinate and data distribution for typical case S_B_4, along with schematic diagrams of the corresponding temporal and spatial frequency spectrum results. In this figure, the purple region represents variation in the spatial position of the anal fin boundary over time at a specific segmentation point, illustrating the temporal sequence of spatial positional changes of the wave line from the viewpoint of individual segmentation points. The temporal Fourier transform essentially converts the description of the signal's overall dynamic variation with respect to time into a representation of the amplitude information of the signal at specific moments with respect to frequency. Figure 18 presents the temporal frequency spectrum results for the same case. The specific procedure for determining the parameters of wave frequency and wave amplitude requires first obtaining the time-series variation at each segmentation point i (i = 1, 2, ..., *NumPts*) along the fin length direction, i.e., obtaining the position $y(t)$ of segmentation point i at times t_1, t_2, ..., t_i. We set the number of segmentation points (*NumPts*) to 100; this value is similar to the number of true fin rays reported for the black ghost knifefish by Albert [34]. Given signal length L (number of instantaneous moments N selected for a single operational case) and sampling frequency F_S (reciprocal of the time interval dt between data points in a single case), the frequency range is determined as $(0, F_S/2)$ with a frequency resolution of $(F_S/2)/(N/2) = F_S/N$. The time vector can be expressed as dt*[0, N−1] (s). Regarding the parameter wave frequency, we treated the anal fin undulation as the spatial propagation of vibration. We identified the maximum value (peak) in the frequency spectrum and then calculated the temporal oscillation frequency f_i (Hz) at each segmentation point i (i = 1, 2, ..., *NumPts*). For the parameter wave amplitude, we calculated the distance d_i from each segmentation point i (i = 1, 2, ..., *NumPts*) on the wave line to the central axis for different instantaneous moments. The mean and SD of each segmentation point and amplitude value were computed and used in the subsequent statistical analyses.

The spatial domain signal was processed to convert the description of the overall dynamic variation of the signal based on spatial coordinates into a representation of the signal's amplitude information at specific instances based on frequency coordinates. Figure 19 presents the coordinates and data distribution of the spatial Fourier transform for operational case S_B_4. The purple region in the figure represents the spatial position distribution of the anal fin boundary at a specific instantaneous moment, illustrating the variation in the spatial position distribution of the wave line from a temporal perspective. The spatial position of the anal fin edge at each instantaneous moment was acquired, i.e., the spatial position $y(x)$ at instance t was obtained for x ($x = x_1, x_2, ..., x_{NumPts}$). Figure 20 shows the spatial frequency spectrum analysis results for the same case. Regarding wavelength, for a given operational case, we identified the spectral maximum (peak) in the spatial Fourier transform results at different instantaneous moments, denoted as f ($f = f_1, f_2, ..., f_{N*dt}$). The numerical values of these peak positions correspond to $1/\lambda$ ($1/\lambda = 1/\lambda_1, 1/\lambda_2, ..., 1/\lambda_N$). The wavelength at each instantaneous moment within the operational case was then calculated as the reciprocal of the respective peak position value, yielding λ ($1/\lambda = 1/\lambda_1, 1/\lambda_2, ..., 1/\lambda_{N*dt}$. The wave number was defined as the number of spatial periods of the sinusoidal-like waveform along the fin. Following the methods of Blake [7] and Shirgaonkar et al. [14] and the assumption that all undulations possess the same wavelength, the wave number was calculated as the maximum fin edge length, max $FinLen_i$ (i = 1, 2, ..., N), divided by the wavelength λ ($\lambda = \lambda_1, \lambda_2, ..., \lambda_N$), i.e., max $FinLen_i/\lambda_i$ (i = 1, 2, ..., N). The mean and SD of the wavelength and wave number across all instantaneous moments within a single operational case were computed and used in the subsequent

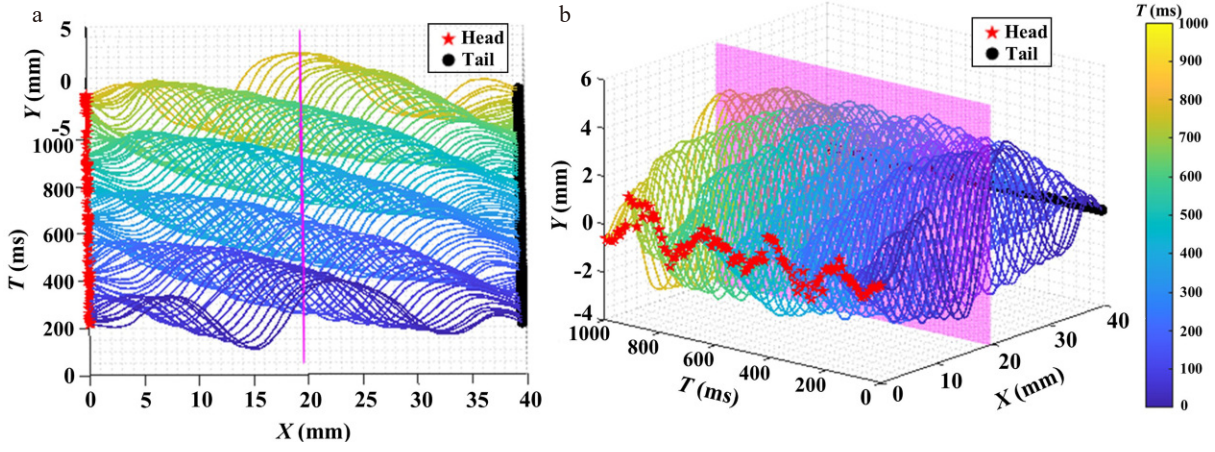

Figure 17 Data structure of the temporal Fourier transform from different perspectives. Case S_B_4, the purple area represents the temporal variation of the spatial position of the lower caudal fin boundary at a certain segmentation point. (a) Planar view. (b) Spatial view.

statistical analyses.

Wave speed was calculated following the computational strategy described by Ruiz-Torres et al. [8]. For a single operational case, the traveling wave speed was determined by first summing the number of times each fin ray segmentation point i (i = 1, 2, ..., *NumPts*) crossed the central axis. This value was then divided by 2 to obtain the number of complete cycles and the results were averaged across all segmentation points i (i = 1, 2, ..., *NumPts*). The resulting values were subsequently multiplied by the fin length and divided by the product of the number of undulations along the fin and the test duration.

We extracted the undulation frequency (f) and wave amplitude (ε) via temporal Fourier transform and obtained the wavelength (λ), wave number (k), and wave speed (V) via spatial Fourier transform. The derived undulation parameters (V, λ, k, f and ε) from this analysis of the 32 operational cases, along with their corresponding dimensionless parameters (λ/L_{fin}, A_{ave}/L_{fin}, and St), are provided in Appendix. The body length of the tested specimens ranged from 51.333 to 109.828 mm, with the corresponding fin length varying from 38.500 to 82.371 mm.

The swimming speed of the black ghost knifefish is typically measured in body lengths per second (BL/s). Figure 21 compares previously reported swimming speed ranges of the knifefish with our findings. Ruiz-Torres et al. [8] observed that, by controlling the incoming flow velocity, the knifefish could achieve swimming speeds ranging from 0 to 2.3 BL/s by adjusting its undulation parameters. In the present study, the measured autonomous swimming speed range was 0.544–1.611 BL/s under conditions free from external disturbances, which falls within the interval reported by Ruiz-Torres et al. [8]. According to Ruiz-Torres et al. [8], at swimming speeds between 0 and 1.24 BL/s, head and tail waves coexist on the anal fin, corresponding to hovering behavior. In contrast, when the flow velocity exceeds 1.38 BL/s, only the head wave is present and the fish swims forward. We observed that the swimming speed range in cases where head and tail waves coexist (0.574–0.880 BL/s) was generally lower than in cases with only a head or tail wave (0.544–1.611 BL/s). However, in case S_B_5 where only a tail wave was present, the swimming speed was lower (0.544 BL/s) than in case L_F_1 (0.574 BL/s) where both waves coexisted. This finding suggests that the waveform pattern of knifefish is not strictly governed by a specific speed threshold, but may be jointly influenced by multiple factors such as genetics and environment. Most swimming speeds measured in our study were below 1 BL/s, consistent with reports by Maciver et al. [20] that the average swimming speed before prey detection was 0.714 BL/s (<1 BL/s). We also found that forward swimming speeds were generally higher than backward swimming speeds. This pattern is consistent with findings from Youngerman et al. [30], who reported

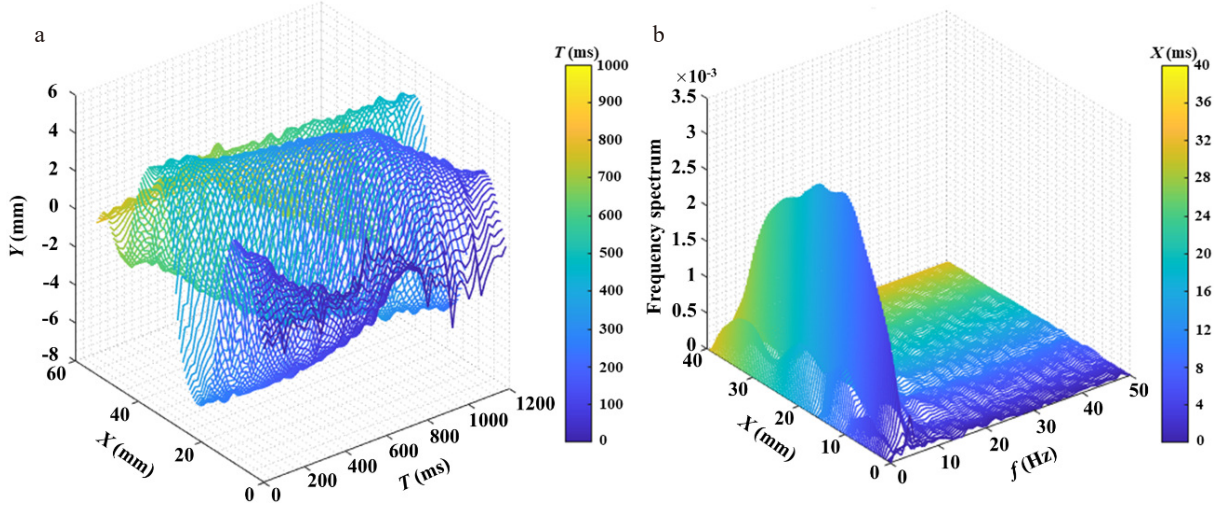

Figure 18 Results of the temporal Fourier transform (Case S_B_4). (a) Temporal diagram. (b) Frequency spectrum.

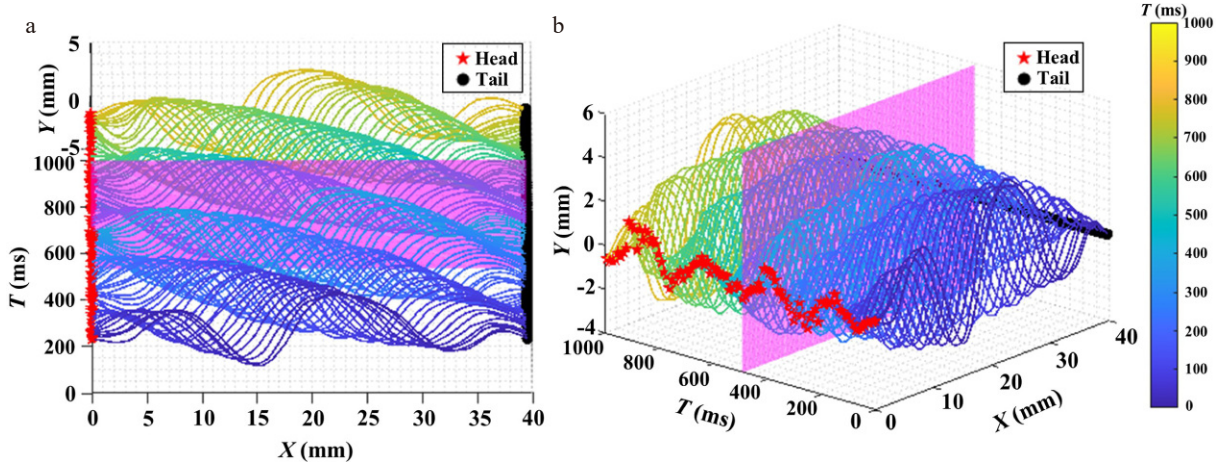

Figure 19 Data structure of the spatial Fourier transform from different perspectives. Case S_B_4, the purple area indicates the spatial position distribution of the boundary of the caudal fin at a certain instant in time. (a) Planar view. (b) Spatial view.

a forward speed of 0.521 ± 0.054 BL/s and a backward speed of 0.294 ± 0.021 BL/s.

Blake [7] reported that the wave number of the black ghost knifefish anal fin ranges from 1.7 to 2.8, with variation due to differences among individuals. Shirgaonkar et al. [14] and Curet et al. [33] both reported that maximum thrust is generated when the fin wave number falls within the range of 2–3. When the wave number is below this range, thrust decreases despite an increase in wave speed; conversely, an excessively high wave number resulted in a reduced wave speed, consequently diminishing thrust. In our study, the wave number range observed during autonomous swimming was 2.113–2.993, with a mean value of 2.278. Only cases L_F_1 and L_F_4 exhibited wave numbers exceeding 2.5, with values of 2.993 and 2.852, respectively. Notably, nodes were present along the anal fin boundary wave line in both of these cases, where the propagating waves resulted from the superposition of inwardly propagating head and tail waves converging at the nodes. When the crests of the two waves approached each other, the total number of anal fin undulations increased. However, when the crests overlapped and the nodes disappeared, the wave number decreased sharply and the anal fin transitioned to a unidirectional wave propagation mode. Blake [7] proposed an empirically observed wavelength-to-fin-length ratio (λ/L_{fin}) of approximately 0.4 for Gymnotidae species. Our experimental results further refine this ratio to a range of 0.347–0.492, providing a more practical reference interval. Ruiz-Torres et al. [8] reported that the undulatory efficiency was 0.5 ± 0.1 at an incoming flow velocity of 1.38 BL/s, but 0.7 ± 0.1 at 2.31 BL/s. At swimming speeds (U) ranging from 0.544 to 1.611 BL/s across our cases the measured undulatory efficiency was 0.488 ± 0.656, which is highly consistent with the findings of Ruiz-Torres et al. [8].

At swimming speeds below 1 BL/s, the cost of transport (i.e., energy consumed per unit mass per unit distance) is not the primary limiting factor because the force generated by the tail wave directly counteracts the fish's motion. Within this speed range (below 1 BL/s), maintaining sufficient lift to offset negative buoyancy and achieve precise posturecontrol are critical. Under higher swimming speeds (approximately ≥ 2 BL/s), the locomotion objective shifts toward maximizing thrust while minimizing drag induced by fin undulations, and the cost of transport is again not the primary consideration. According to the principle of dynamic similarity, the swimming speed of the knifefish is not independent of its undulation parameters; rather, it is a function determined by dimensionless combinations of these parameters. To investigate the influence of various undulation parameters on swimming speed, we plotted the relationships between dimensionless parameters—wave number (k), normalized wavelength (λ/L_{fin}), normalized wave amplitude (A_{ave}/L_{fin}), wave frequency (f), wave speed (V), and undulatory efficiency (η)—and swimming speed (U) for the 32 operational cases (Fig. 22). As shown, wave frequency (f = 5.638 ±

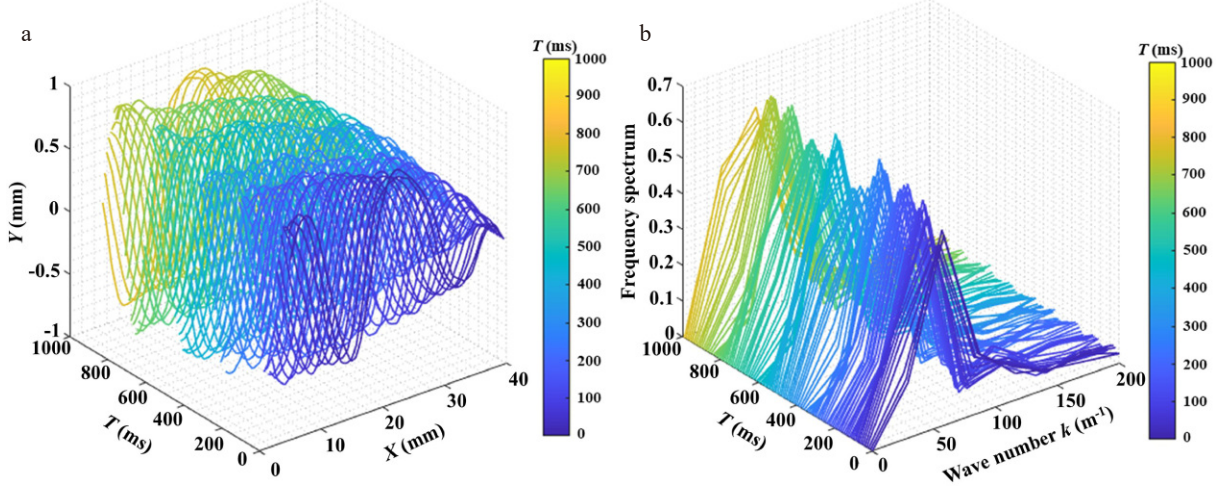

Figure 20 Results of the spatial Fourier transform (Case S_B_4). (a) Temporal diagram. (b) Frequency spectrum.

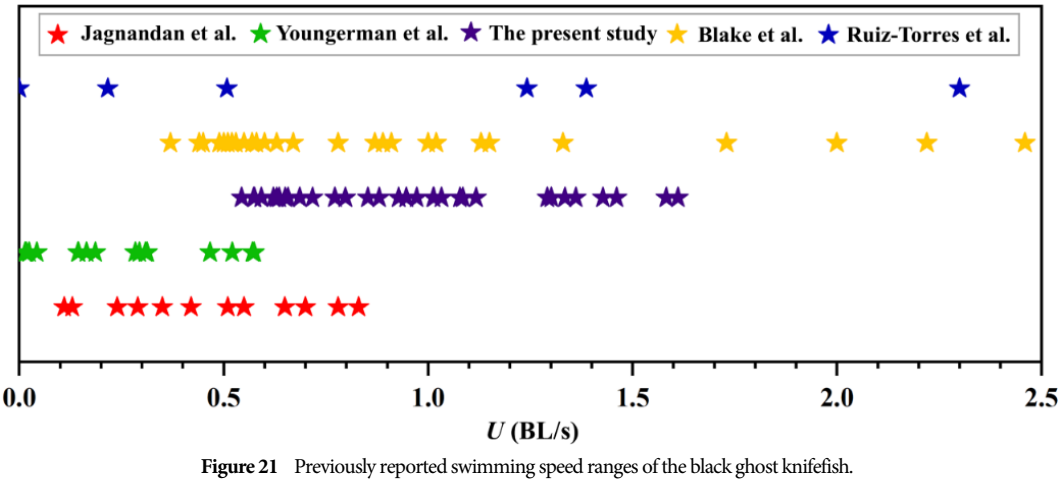

Figure 21 Previously reported swimming speed ranges of the black ghost knifefish.

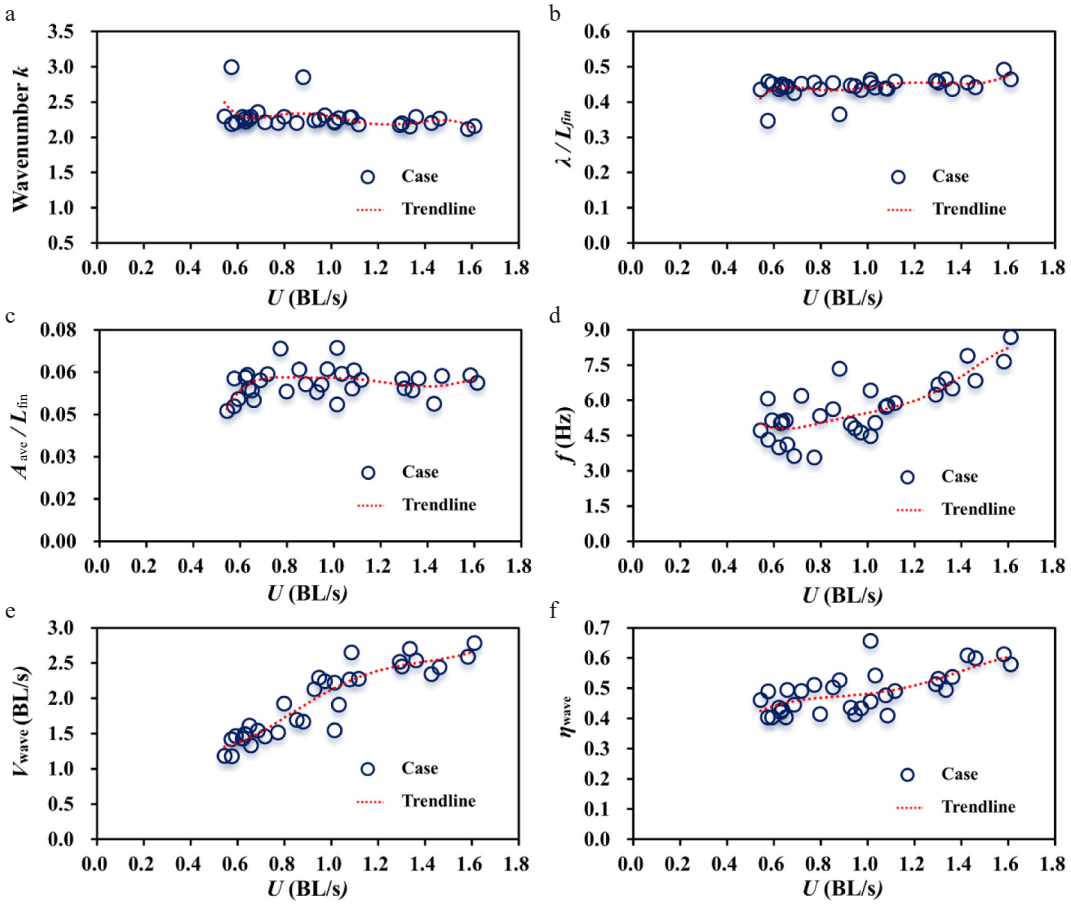

Figure 22 Relationship between swimming speed and various undulation parameters. (a) k. (b) λ/L_{fin}. (c) A_{ave}/L_{fin}. (d) f. (e) V_{wave}. (f) η_{wave}.

1.233 Hz) was the most reliable parameter for predicting swimming speed. In contrast, wave amplitude A_{ave}/L_{fin} = 0.056 ± 0.0051) and wave number (k = 2.278 ± 0.175) did not significantly correlate with speed and did not undergo substantial changes with varying velocity, indicating their limited role. Given these findings, wave frequency is the key undulation parameter controlling the swimming speed in the black ghost knifefish.

The propulsive undulation mode of the anal fin varies with changes in its kinematic parameters. Multiple regression analysis was performed to systematically evaluate the interrelationships among these undulation parameters, including wave speed (V), swimming speed (U), dimensionless wavelength (λ/L_{fin}), dimensionless maximum wave amplitude (A_{max}/L_{fin}), dimensionless mean wave amplitude (A_{ave}/L_{fin}), wave number (k), wave frequency (f), wave efficiency (η), and Strouhal number (St). The undulation parameters of the anal fin edge were continuous variables and contained no outliers; the parameter variables used for comparison were derived from the same population. Figure 23 presents of heatmap of the correlations between variables and Table 2 presents the corresponding significance values. No correlation coefficients between any two undulation parameters reached an extreme value of 0 or 1, suggesting that these parameters are not mutually independent but form an operational range within the anal fin kinematic parameter space that both coordinate and constrain each another. Ruiz-Torres et al. [8] noted that when the swimming speed of the knifefish increases to approximately 1 BL/s, the wave speed (V) monotonically increases with swimming speed (U). Our data show a strong positive correlation (0.91) between U and V, indicating that V tends to rise as U increases (U = 0.544–1.611 BL/s), although a strictly monotonic relationship could not be confirmed. Wave frequency (f) showed relatively strong positive correlations of 0.67 and 0.76 with V and U, respectively. This findings supports that adjusting the wave frequency is likely an effective means of controlling the increase in swimming speed. A moderate positive correlation was observed between undulatory efficiency (η) and parameters U and f, which inherently arises because η is functionally expressed in terms of parameters U and V. The wave amplitude parameters (A_{max}/L_{fin} and A_{ave}/L_{fin}) did not exhibit significant correlations, indicating that they did not undergo substantial changes in response to other parameters. As we idealized all undulations as having the same wavelength, the wave number (k) was calculated as the ratio of the maximum fin edge length to the wavelength. Accordingly, a strong negative correlation (−0.97) was observed between k and λ/L_{fin}. We used η and the Strouhal number (St) to evaluate swimming performance, with a higher η and a lower St implying better propulsive performance. The undulation parameters V, U, λ/L_{fin}, A_{max}/L_{fin}, k, and f exhibited opposite signs in their correlations with η and St, indirectly indicating a moderate negative correlation (−0.43) between η and St. This relationship implies that the ideal extreme values of η = 1 and St = 0 cannot be simultaneously achieved. Overall, these findings indicate that the swimming performance of the black ghost knifefish is not determined by a single parameter in isolation, but is collectively regulated by dimensionless functions of the various undulation parameters.

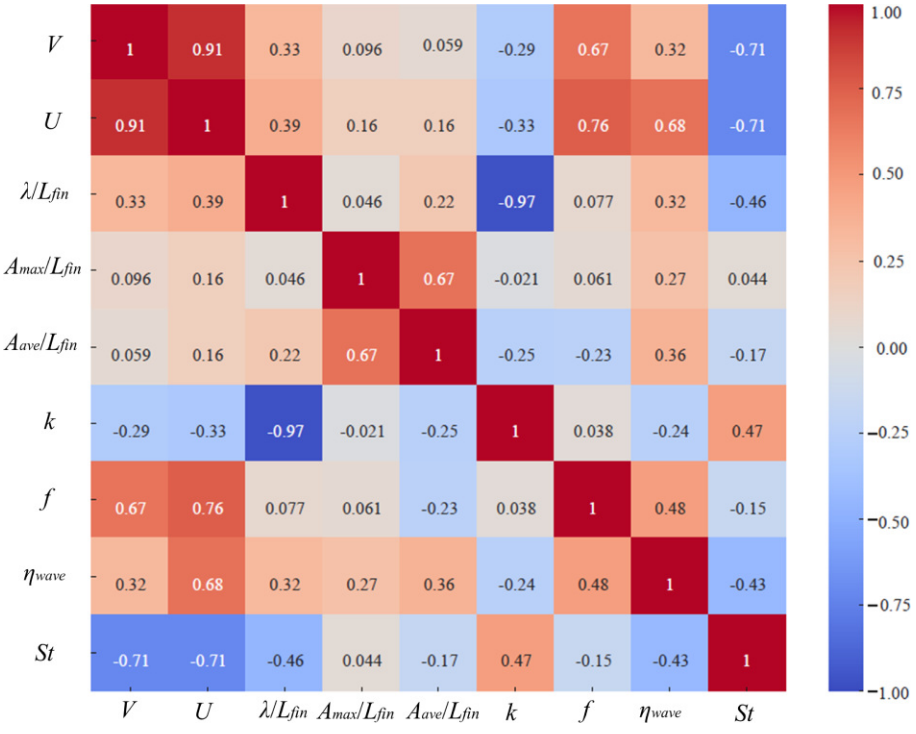

Figure 23 Heatmap of correlation coefficients between undulation parameters determined by Pearson correlation analysis. Red indicates a positive correlation, blue indicates a negative correlation, and the color intensity reflects the magnitude of the correlation coefficient.

Table 2 Significance (*p*-values) of relationships between various parameters assessed by Pearson correlation analysis.

	V	U	λ/L_{fin}	A_{max}/L_{fin}	A_{ave}/L_{fin}	k	f	η_{wave}	St
V	0.000***	0.003***	0.061*	0.601	0.749	0.102	0.004***	0.072*	0.001***
U	0.003***	0.000***	0.025**	0.378	0.391	0.069*	0.003***	0.004***	0.002***
λ/L_{fin}	0.061*	0.025**	0.000***	0.801	0.228	0.001**	0.677	0.078*	0.008***
A_{max}/L_{fin}	0.601	0.378	0.801	0.000***	0.004***	0.910	0.739	0.134	0.810
A_{ave}/L_{fin}	0.749	0.391	0.228	0.004***	0.000***	0.169	0.212	0.043**	0.365
k	0.102	0.069*	0.001**	0.910	0.169	0.000***	0.838	0.181	0.007***
f	0.004***	0.003***	0.677	0.739	0.212	0.838	0.000***	0.006***	0.410
η_{wave}	0.072*	0.004***	0.078*	0.134	0.043**	0.181	0.006***	0.000***	0.014**
St	0.001***	0.002***	0.008***	0.810	0.365	0.007***	0.410	0.014**	0.000***

Note: * $p < 0.10$, ** $p < 0.05$, and *** $p < 0.01$.

4 Conclusion

By performing morphological and kinematic analyses of anal fin propulsion in the black ghost knifefish, this study makes several important contributions to the literature. We found that the anal fin attaches obliquely to the body with a streamlined configuration, facilitating the generation of both vertical and horizontal force components during propulsion. The high maneuverability of this species stems from precise regulation of the traveling wave direction and undulation mode of its anal fin. Keys to achieving complex motion, including hovering, are formation of an asymmetric waveform, superposition of counter-propagating waves, and modulation of wave nodes. We demonstrated a clear functional relationship between swimming speed and undulatory parameters, with wave frequency being the most critical predictor. Propulsion performance was jointly determined by the synergy and constraints among all motion parameters within their operational ranges. These findings provide important quantitative evidence and theoretical references for understanding the biomechanics of undulatory fin propulsion and guiding the design of bioinspired systems. Notably, our data were limited to high-precision visual recordings of autonomous swimming of the black ghost knifefish in still water. Future studies should consider the complexity of the natural habitat and investigate obstacle avoidance strategies and motion pattern adaptability in confined spaces from a three-dimensional perspective. Further research exploring the influence of unsteady flow fields and complex hydrodynamic environments on locomotor behavior is also warranted.

Acknowledgements

The authors would like to thank the Animal Protection Society of Northwestern Polytechnical University for their assistance with fish husbandry.

Author contribution statement

Ze-Jun Liang: Writing – original draft & Formal analysis (equal).

Peng Xu: Writing – review & editing (equal). Yi-Wei Fan and Dong-Yang Chen: Data curation and investigation (equal). Kun-De Yang: Investigation and Validation (equal). All the authors have approved the final manuscript.

Data availability

The data that support the findings of this study are available from the corresponding author upon reasonable request.

Declaration of competing interest

All the contributing authors report no conflicts of interest in this work.

Ethical approval

This work was approved by the Animal Protection Society of Northwestern Polytechnical University.

Funding

This work is granted by the Postdoctoral Innovation Fund of Northwestern Polytechnical University Taicang Yangtze River Delta Research Institute (Grant Nos. 14005-5140250013, 14005-5140250014), the National Natural Science Foundation of China (Grant No. 52471342), the basic Research Programs of Taicang (Grant No. TC2024JC06), and Gusu Youth Innovation Leading Talent Project (Grant No. ZXL2023168).

Use of AI statement

None

Appendix

The exact values of data described in the article, as most data were presented as figures.

Table A1 Detailed list of undulation parameters.

Case	V (mm/s)	λ (mm)	k	f (Hz)	ε_{max} (mm)
S_F_1	115.96 ± 5.78	18.110 ± 2.228	2.223 ± 0.123	6.421 ± 0.326	3.126 ± 0.391
S_F_2	140.89 ± 6.62	17.429 ± 1.481	2.286 ± 0.085	5.772 ± 0.574	3.821 ± 0.271
S_F_3	132.50 ± 7.42	17.104 ± 2.241	2.291 ± 0.131	6.503 ± 2.513	3.775 ± 0.145
S_F_4	122.04 ± 5.61	17.717 ± 1.683	2.281 ± 0.095	5.714± 0.268	3.308 ± 0.240
S_F_5	171.42 ± 8.57	24.916 ± 2.317	2.200 ± 0.093	7.889 ± 1.697	4.929 ± 0.479
S_F_6	183.21 ± 7.51	26.127 ± 5.513	2.113 ± 0.211	7.653 ± 1.326	5.164 ± 0.935
S_F_7	137.95± 3.58	20.091 ± 1.728	2.247 ± 0.086	4.804 ± 1.513	4.262 ± 0.508
S_F_8	131.81 ± 7.11	20.722 ± 2.321	2.240 ± 0.112	4.989 ± 2.892	4.162 ± 0.126
S_B_1	77.32 ± 4.33	17.579 ± 1.371	2.223 ± 0.078	5.102 ± 1.273	3.605 ± 0.098
S_B_2	101.64 ± 5.18	17.296 ± 1.401	2.289 ± 0.081	5.333 ± 2.514	3.650 ± 0.265
S_B_3	72.31 ± 3.68	18.080 ± 2.242	2.290 ± 0.124	4.125 ± 1.269	3.465 ± 0.474
S_B_4	75.21 ± 3.68	17.271 ± 3.696	2.289 ± 0.214	4.000 ± 1.085	3.691 ± 0.200
S_B_5	61.25 ± 3.12	16.958 ± 2.645	2.294 ± 0.156	4.719 ± 0.478	2.858 ± 0.239
S_B_6	60.32 ± 3.37	17.620 ± 2.608	2.185 ± 0.148	4.323 ± 1.583	3.580 ± 0.799
S_B_7	109.63 ± 4.06	24.693 ± 5.507	2.200 ± 0.223	3.571 ± 0.961	5.527 ± 0.294
S_B_8	109.65 ± 6.14	24.134 ± 2.727	2.205 ± 0.113	4.468 ± 0.660	5.571 ± 0.276
L_F_1	149.14 ± 5.52	27.316 ± 6.583	2.993 ± 0.241	6.061 ± 1.370	7.327 ± 0.499
L_F_2	258.14 ± 9.46	35.032 ± 5.395	2.265 ± 0.154	6.830 ± 1.149	7.614 ± 0.361
L_F_3	250.59 ± 9.52	34.966 ± 6.329	2.196 ± 0.181	6.667 ± 1.413	8.385 ± 0.216
L_F_4	173.14 ± 9.69	28.368 ± 3.518	2.852 ± 0.124	7.340 ± 2.700	7.277 ± 0.471
L_F_5	231.72 ± 8.98	35.003 ± 7.456	2.181 ± 0.213	5.887 ± 1.723	6.597 ± 0.431
L_F_6	250.69 ± 9.04	32.359 ± 3.204	2.153 ± 0.099	6.909 ± 2.066	6.503 ± 0.519
L_F_7	247.56 ± 8.13	33.928 ±6.616	2.173 ± 0.195	6.231 ± 1.296	6.957± 0.241
L_F_8	255.98± 6.34	32.018 ± 4.579	2.155 ± 0.143	8.687 ± 3.613	6.592 ± 0.250
L_B_1	169.41 ± 6.09	35.002 ± 3.920	2.353 ± 0.112	3.636 ± 1.312	7.659 ± 0.505
L_B_2	170.19 ± 9.53	34.989 ± 3.604	2.260 ± 0.103	5.152 ± 0.861	8.612 ± 0.392
L_B_3	201.96 ± 8.32	35.014 ± 3.396	2.268 ± 0.097	5.040 ± 0.402	8.174 ± 0.507
L_B_4	152.56 ± 8.54	35.412 ± 3.966	2.212 ± 0.112	6.192 ± 1.680	7.452 ± 3.163
L_B_5	181.26 ± 8.70	36.394 ± 3.931	2.203 ± 0.108	5.623 ± 1.513	7.846 ± 3.431
L_B_6	241.51 ± 6.54	35.001 ± 3.395	2.307 ± 0.097	4.621 ± 0.689	6.455 ± 0.492
L_B_7	154.86 ± 5.52	34.426 ± 3.270	2.256 ± 0.095	5.023 ± 1.453	6.268 ± 2.475
L_B_8	152.23 ± 6.54	35.194 ± 4.434	2.213 ± 0.126	5.146 ± 1.286	7.967 ± 4.742

Table A2 Dimensionalization calculation results of undulation parameters.

Case	Average speed (mm/s)	Average speed (BL/s)	λ/L_{fin}	A_{max}/L_{fin}	A_{ave}/L_{fin}	η_{wave}	St
S_F_1	52.886 ± 2.112	1.013 ± 0.040	0.463	0.080	0.049	0.456	0.231
S_F_2	57.662 ± 1.628	1.085 ± 0.031	0.437	0.096	0.061	0.409	0.242
S_F_3	71.147 ± 2.006	1.362 ± 0.038	0.436	0.096	0.058	0.537	0.207
S_F_4	58.065 ± 1.962	1.078 ± 0.036	0.438	0.082	0.054	0.476	0.215
S_F_5	104.351 ± 2.972	1.427 ± 0.041	0.454	0.090	0.049	0.609	0.202
S_F_6	112.101 ± 3.684	1.582 ± 0.052	0.492	0.097	0.059	0.612	0.214
S_F_7	57.031 ± 2.609	0.947 ± 0.043	0.445	0.094	0.056	0.413	0.211
S_F_8	57.438 ± 2.708	0.928 ± 0.044	0.446	0.090	0.053	0.436	0.213
S_B_1	33.138 ± 1.255	0.636 ± 0.024	0.450	0.092	0.054	0.429	0.327
S_B_2	42.112 ± 2.119	0.798 ± 0.040	0.437	0.092	0.053	0.414	0.266
S_B_3	35.759 ± 3.481	0.658 ± 0.064	0.443	0.085	0.050	0.495	0.236
S_B_4	32.789 ± 2.772	0.622 ± 0.053	0.437	0.093	0.058	0.436	0.280
S_B_5	28.211 ± 1.023	0.544 ± 0.020	0.436	0.073	0.046	0.461	0.300
S_B_6	29.553 ± 3.453	0.576 ± 0.067	0.458	0.093	0.058	0.490	0.325
S_B_7	55.958 ± 2.121	0.772 ± 0.029	0.454	0.102	0.068	0.510	0.237
S_B_8	71.921 ± 4.558	1.014 ± 0.064	0.453	0.105	0.069	0.656	0.227
L_F_1	60.271 ± 3.475	0.574 ± 0.033	0.347	0.093	0.048	0.404	0.379
L_F_2	154.602 ± 5.129	1.461 ± 0.048	0.441	0.083	0.059	0.599	0.205
L_F_3	133.247 ± 4.261	1.302 ± 0.042	0.455	0.095	0.054	0.532	0.209
L_F_4	91.232 ± 4.201	0.880 ± 0.041	0.365	0.098	0.056	0.527	0.348
L_F_5	113.727 ± 2.017	1.117 ± 0.020	0.458	0.097	0.057	0.491	0.226
L_F_6	123.984 ± 4.611	1.335 ± 0.050	0.464	0.104	0.053	0.495	0.208
L_F_7	126.993 ± 4.632	1.292 ± 0.047	0.460	0.089	0.058	0.513	0.209
L_F_8	148.271 ± 5.823	1.611 ± 0.063	0.464	0.094	0.056	0.579	0.227
L_B_1	75.367 ± 3.941	0.686 ± 0.036	0.425	0.092	0.057	0.445	0.227
L_B_2	68.643 ± 4.866	0.651 ± 0.046	0.442	0.083	0.053	0.403	0.317
L_B_3	109.371 ± 2.965	1.033 ± 0.028	0.441	0.096	0.059	0.542	0.217
L_B_4	74.917 ± 3.332	0.717 ± 0.032	0.452	0.101	0.059	0.491	0.383
L_B_5	91.146 ± 2.185	0.853 ± 0.020	0.454	0.102	0.061	0.503	0.301
L_B_6	104.706 ± 3.934	0.972 ± 0.037	0.433	0.092	0.061	0.434	0.218
L_B_7	65.265 ± 1.112	0.630 ± 0.011	0.443	0.101	0.059	0.421	0.353
L_B_8	61.522 ± 1.365	0.592 ± 0.013	0.452	0.083	0.050	0.404	0.328

References

[1] Webb, P. W. (1984). Form and function in fish swimming. *Sci. Am.* 251, 72–83.

[2] Liang, Z. J., Guo, C. Y., Han, Y., Xu, P., Yu, Y. Y. (2023). Kinematic and hydrodynamic mechanisms of *Misgurnus anguillicaudatus* during routine turning. *Phys. Fluids* 35, 055120.

[3] Mwaffo, V., Zhang, P., Cruz, S. R., Porfiri, M. (2017). Zebrafish swimming in the flow: a particle image velocimetry study. *PeerJ.* 5, e4041.

[4] Witt, W. C., Wen, L., Lauder, G. V. (2015). Hydrodynamics of C-start escape responses of fish as studied with simple physical models. *Integr. Comp. Biol.* 55, 728–739.

[5] Adhikari, D., Longmire, E. K. (2013). Infrared tomographic PIV and 3D motion tracking system applied to aquatic predator–prey interaction. *Meas. Sci. Technol.* 24, 024011.

[6] Shih, A. M., Mendelson, L., Techet, A. H. (2017). Archer fish jumping prey capture: kinematics and hydrodynamics. *J. Exp. Biol.* 220, 1411–1422.

[7] Blake, R. W. (1983). Swimming in the electric eels and knifefishes. *Can. J. Zool.* 61, 1432–1441.

[8] Ruiz-Torres, R., Curet, O. M., Lauder, G. V., MacIver, M. A. (2013). Kinematics of the ribbon fin in hovering and swimming of the electric ghost knifefish. *J. Exp. Biol.* 216, 823–834.

[9] Sefati, S., Neveln, I., MacIver, M. A., Fortune, E. S., Cowan, N. J. (2012). Counter-propagating waves enhance maneuverability and stability: a bio-inspired strategy for robotic ribbon-fin propulsion. In *2012 4th IEEE RAS & EMBS International Conference on Biomedical Robotics and Biomechatronics (BioRob).* Rome, Italy, p 1620–1625.

[10] Sefati, S., Neveln, I. D., Roth, E., Mitchell, T. R. T., Snyder, J. B., MacIver, M. A., Fortune, E. S., Cowan, N. J. (2013). Mutually opposing forces during locomotion can eliminate the tradeoff between maneuverability and stability. *Proc. Natl. Acad. Sci.* USA 110, 18798–18803.

[11] Neveln, I. D., Bale, R., Bhalla, A. P. S., Curet, O. M., Patankar, N. A., MacIver, M. A. (2014). Undulating fins produce off-axis thrust and flow structures. *J. Exp. Biol.* 217, 201–213.

[12] Ortega-Jiménez, V. M., Sanford, C. P. (2021). Beyond the Kármán gait: knifefish swimming in periodic and irregular vortex streets. *J. Exp. Biol.* 224, jeb238808.

[13] Hawkins, O. H., Ortega-Jiménez, V. M., Sanford, C. P. (2022). Knifefish turning control and hydrodynamics during forward swimming. *J. Exp. Biol.* 225, jeb243498.
[14] Shirgaonkar, A. A., Curet, O. M., Patankar, N. A., MacIver, M. A. (2008). The hydrodynamics of ribbon-fin propulsion during impulsive motion. *J. Exp. Biol.* 211, 3490–3503.
[15] Liang, Z. J., Chen, D. Y., Xu, P., Dong, G. J. (2025). Three-dimensional flow field analysis of biomimetic undulating fins: a comparative study of fin morphologies. *Phys. Fluids* 37, 101907.
[16] Liang, Z. J., Chen, D. Y., Xu, P., Dong, G. J. (2026). Three-dimensional hydrodynamic characteristics of the bio-inspired undulating fin under various angular amplitude undulation modes. *Ocean Eng.* 344, 123646.
[17] Maciver, M. A., Sharabash, N. M., Nelson, M. E. (2001). Prey-capture behavior in gymnotid electric fish: motion analysis and effects of water conductivity. *J. Exp. Biol.* 204, 543–557.
[18] Curet, O. M., Patankar, N. A., Lauder, G. V., MacIver, M. A. (2011). Aquatic manoeuvering with counter-propagating waves: a novel locomotive strategy. *J. Roy. Soc. Interface* 8, 1041–1050.
[19] MacIver, M. A., Patankar, N. A., Shirgaonkar, A. A. (2010). Energy-information trade-offs between movement and sensing. *PLoS Comput. Biol.* 6, e1000769.
[20] MacIver, M. A., Fontaine, E., Burdick, J. W. (2004). Designing future underwater vehicles: principles and mechanisms of the weakly electric fish. *IEEE J. Oceanic Eng*. 29, 651–659.
[21] Lamas, M. I., Rodríguez, J. D., Rodríguez, C. G., González, P. B. (2011). Three-dimensional CFD analysis to study the thrust and efficiency of a biologically-inspired marine propulsor. *Pol. Marit. Res.* 18, 10–16.
[22] Zhang, Y. H., He, J. H., Low, K. H. (2012). Parametric study of an underwater finned propulsor inspired by bluespotted ray. *J. Bionic Eng.* 9, 166–176.
[23] Quan, X. Y., Zhao, X. M., Zhang, S. J., Zhou, J., Yu, N., Hou, X. Y. (2021). Research on the undulatory motion mechanism of seahorse based on dynamic mesh. *Appl. Bionics Biomech.* 2021, 2807236.
[24] Liu, H. L., Curet, O. (2018). Swimming performance of a bio-inspired robotic vessel with undulating fin propulsion. *Bioinspir. Biomim.* 13, 056006.
[25] Bai, Y. Q., Zhang, J., Zhai, S. C., Zhang, G. P. (2021). Investigations on vortex structures for undulating fin propulsion using phase-locked digital particle image velocimetry. *J. Hydrodyn.* 33, 572–582.
[26] Shirgaonkar, A. A., MacIver, M. A., Patankar, N. A. (2009). A new mathematical formulation and fast algorithm for fully resolved simulation of self-propulsion. *J. Comput. Phys.* 228, 2366–2390.
[27] Uddin, M. I. (2022). Swimming Control of an Underwater Vessel with Elongated Ribbon Fin Propulsion. Ph. D. Dissertation. Florida Atlantic University, Boca Raton, FL, USA.
[28] Drago III, A. C. (2024). Exploiting Asymmetric Velocity Profiles to Improve Undulatory Propulsion of Fin-Based Underwater Vehicles. Master Degree Thesis. Drexel University, Philadelphia, PA, USA.
[29] Jagnandan, K., Sanford, C. P. (2013). Kinematics of ribbon-fin locomotion in the bowfin, Amia calva. *J. Exp. Zool. Part A: Ecol. Genet. Physiol* 319, 569–583.
[30] Youngerman, E. D., Flammang, B. E., Lauder, G. V. (2014). Locomotion of free-swimming ghost knifefish: anal fin kinematics during four behaviors. *Zoology* 117, 337–348.
[31] Albert, J. S., Crampton, W. G. R. (2005). Diversity and phylogeny of neotropical electric fishes (gymnotiformes). In Electroreception. Bullock, T. H., Hopkins, C. D., Popper, A. N., Fay, R. R., Eds. New York: Springer, p 360–409.
[32] Jayne, B. C., Lauder, G. V. (1995). Speed effects on midline kinematics during steady undulatory swimming of largemouth bass, Micropterus salmoides. *J. Exp. Biol.* 198, 585–602.
[33] Curet, O. M., Patankar, N. A., Lauder, G. V., MacIver, M. A. (2011). Mechanical properties of a bio-inspired robotic knifefish with an undulatory propulsor. *Bioinspir. Biomim.* 6, 026004.
[34] Albert, J. S. (2001). Species diversity and phylogenetic systematics of American knifefishes (Gymnotiformes, Teleostei). Ann Arbor, Mich: Division of Ichthyology, Museum of Zoology, University of Michigan.